Dynamic performance analysis of reflective semiconductor optical amplifiers

Pluk, E.G.C.

Award date:
2006

Eindhoven University of Technology
Faculty of Electrical Engineering
Division of Telecommunication Technology and Electromagnetics
Electro-optical Communication (ECO) Group

DYNAMIC PERFORMANCE ANALYSIS OF REFLECTIVE SEMICONDUCTOR OPTICAL AMPLIFIERS

by E.G.C. Pluk

Master of Science Thesis
carried out from March 2005 to March 2006

Supervisor:
dr. ir. H. de Waardt

Graduation professor:
prof. ir. A.M.J. Koonen

Abstract

The BroadBand Photonics project develops reconfigurable optical access networks. Key component for these networks are the dynamically reconfigurable wavelength router and the colourless Optical Network Unit (ONU). In the ONU the upstream communication is provided by direct modulation of a Reflective Semiconductor Optical Amplifier (RSOA). The gain of the RSOA is modulated, so it will impose the upstream data on an incoming CW signal. The assignment of this project is to investigate if it is possible to use a Reflective Semiconductor Optical Amplifier to modulate an incoming CW-signal.

An investigation of the theory of SOAs is performed. Interactions between photons and electrons are described, and the rate-equations are deducted for bulk and Multiple Quantum Well (MQW) active regions. A short dynamic analysis is performed based on the rate equations. Also the model used in the simulations is described.

Static simulations and measurements are performed. The static measurement results show slightly disappointing results for the bulk device, compared with the simulation results. However, the results for the MQW device are promising. Afterwards model parameters are modified, trying to obtain matching between the simulation results and the measurement results. If this matching is obtained, the model will give a better representation of reality. After this matching, dynamic simulations are performed. A 625 Mbit/s modulated signal could be detected error-free for the bulk device. For the MQW device, 1 Gbit/s modulation gave almost error-free transmission.

Dynamic measurements are performed on a commercially available device. The obtained results look much better than the results from simulations. A bitrate of 1.25 Gbit/s could be easily obtained. It is even possible to modulate the RSOA with 2.5 Gbit/s, still guaranteeing error-free detection. For a bitrate of 1.25Gbit/s and input CW power of -28 dBm the received power, for a Bit-Error-Rate (BER) of 10^{-9} is as low as -24 dBm, when a 1.25 Gbit transceiver module is used for the detection. Obtained Extinction Ratio and Optical Signal-to-Noise Ratio also show good results.

Contents

List of Figures

List of Tables

List of Abbreviations

ASE	Amplified Spontaneous Emission
AWG	Arrayed Waveguide Grating
BER	Bit-Error-Rate
BPF	Band-Pass Filter
CW	Continuous Wave
DC	Direct Current
DWDM	Dense Wavelength Division Multiplexed
FTTH	Fiber To The Home
LDC	Laser Diode Controller
MQW	Multiple Quantum Well
MZ	Mach-Zehnder
OLT	Optical Line Termination
ONU	Optical Network Unit
OSA	Optical Spectrum Analyser
OSNR	Optical Signal-to-Noise Ratio
PCB	Printed Circuit Board
PPG	Pulsed Pattern Generator
PRBS	Pseudo-Random Binary Sequence
QD	Quantum Dot
RSOA	Reflective Semiconductor Optical Amplifier
SCH	Separate Confinement Heterostructure
SMA	SubMiniature version A
SOA	Semiconductor Optical Amplifier
TEC	TEmperature Controller
TLLM	Transmission-Line Laser Model
TW	Travelling Wave
WDM	Wavelength Division Multiplexed

Chapter 1

Introduction

This graduation project is performed in the scope of a project with several industrial partners and educational groups, all located within the Netherlands. The project is called "BBPhotonics", which stands for dynamically reconfigurable broadband photonic access networks [1], and is funded by the Freeband Communication community.

The target of the BBPhotonics project will be explained first, followed by a description of the assignment for this project.

1.1 The BBPhotonics Project

The BBPhotonics project develops a reconfigurable access network, providing the user with congestion-free acces to abundant amounts of information. By enabling the network operator to easily and remotely reconfigure his access network, the capacity distribution across the users can timely be adapted to his varying service demands. Optical fibre carrying multiple wavelength channels is chosen for the broadband flexible network infrastructure. Putting emphasis on low costs, which is a crucial factor for success in the access market, reconfigurable access network architectures and access network modules will be investigated. Compact low-power photonic integrated circuits and intelligent network reconfiguration mechanisms are key research items in the project. A demonstrator at one of the start-up company partners will show the power of this innovative access network concept. Important for the success of this design are a reconfigurable wavelength router based on a relative new technology, and a smart solution providing the upstream data communication, leading to a cheap and colourless Optical Network Unit.

To make the concept clear, a reference network (figure 1.1) has been designed [2]. This reference network will give a clear starting point for the development of several components.

This reference network has a powerful set of features [3]. It provides 20 wavelength channels, separated in 10 upstream and 10 downstream channels. The wavelength channels are spaced by 200 GHz, and are located in pairs of up and downstream channels (figure 1.2). Every channel can provide up to 10 Gigabit Ethernet. 4 remote nodes are connected via a single fiber ring network, each remote node connects up to 256 users. Bidirectional amplifiers allow bidirectional traffic over the fiber ring, which also improves the redundancy of the network. The distance between two remote nodes is limited to 20 km, the distance between the user and the remote node is limited to 5 km. A control channel is embedded in the system, to control the dynamic reconfigurability.

Some wavelength channels are used for downstream data transport, these are generated and modulated in the Optical Line Termination (OLT) module and detected at the user. The OLT

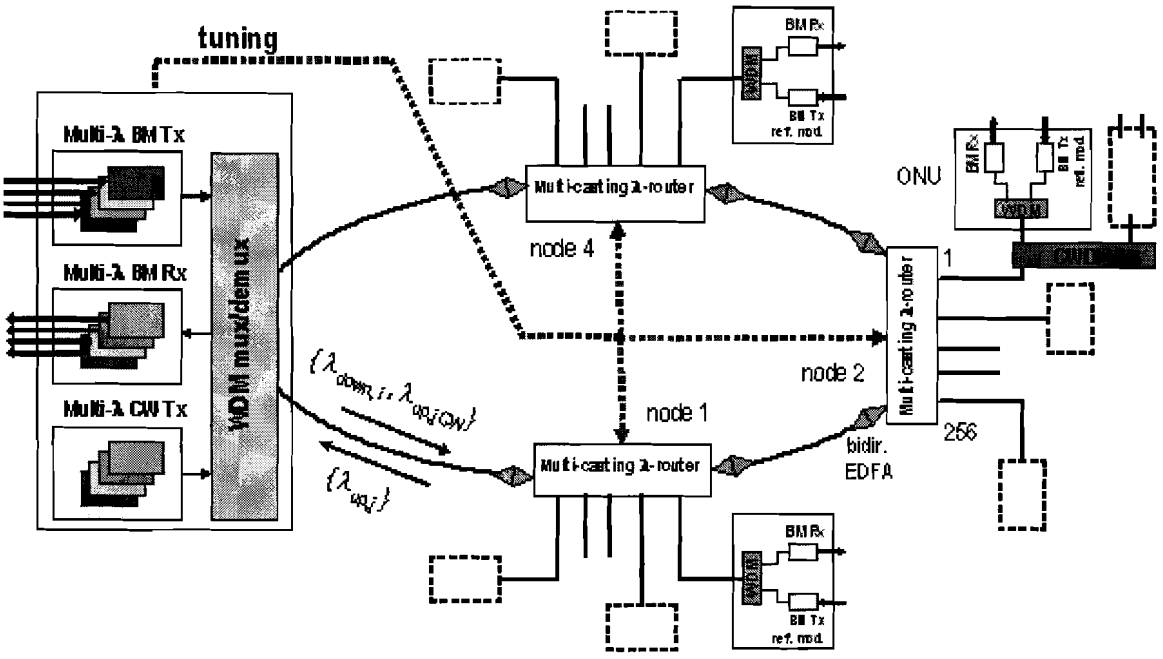

Figure 1.1: Schematic view of the reference network architecture.

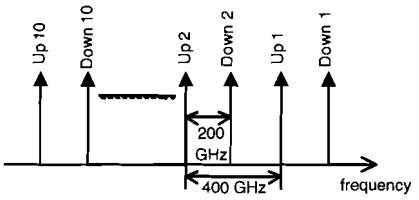

Figure 1.2: Wavelength architecture of the reference network.

also generates Continuous Wave (CW) signals for the wavelength channels that are reserved for upstream communication. In the Optical Network Unit (ONU), the upstream data is imposed on one of these CW signals, and the modulated signal is returned to the OLT. In the eventual system the OLT transfers information from/to the feeder network, which will probably be a DWDM high speed optical Wide Area Network.

According to the project description, the capacity distribution can be timely adapted. In the reference network, this reconfigurability is implemented in the wavelength router. In the wavelength router, the incoming wavelength-channels are distributed to several users, or they are passed on to the next router. In order to make this routing dynamical and controllable, a new concept will be used. Micro-ringresonators can be used to transfer optical power between two nearby waveguides. The resonance frequency of this resonator can be controlled by thermal tuning. The amount of power, transferred by the ringresonator, can be adjusted by slight detuning. The wavelength router works in both directions, so it is possible to use a single fibre ring structure.

The last important part of the network is the transceiver module, placed at every user. This module is also called the Optical Network Unit (ONU). The task of the ONU is to receive downstream information, and to send upstream information. The assignment of this project is strongly linked to the ONU, therefore the functionality of the ONU is described in more detail below.

1.1.1 The Optical Network Unit

In the network as described above, it is not sure which wavelength channel(s) will be used to communicate with the user. Also the required dynamical reconfiguration can cause a sudden change in wavelength channels received by the user. Thus for cost-efficiency reasons and for easy controlling it is advantageous to avoid the use of wavelength-specific components. The functionality of the ONU can be divided into two main parts. First the incoming downstream optical signal has to be received. Doing this in a wavelength-agnostic way is actually straightforward: a normal wide-band photodetector can be used. The second functionality is most complicated part of the ONU: the generation of an upstream data signal. This also has to be done without wavelength-specific components. A solution is proposed where a CW signal is received from the OLT, in the ONU it is modulated and amplified, and afterwards returned upstream, carrying the upstream data. For the modulation and amplification of signals over a wide range of wavelengths, a Semiconductor Optical Amplifier (SOA) seems suitable. A single optical fibre is used to carry all three signals (downstream data at λ_1, downstream CW at λ_2 and upstream data at λ_2 in the opposite direction), so the wavelengths have to be separated first. As seen earlier (figure 1.2), the upstream and downstream channels are designed as couples on a frequency-grid, so a fixed frequency-difference separates the upstream and downstream of couple 1, but also the upstream of couple 1 and the downstream of couple 2 are separated by this difference. Given the use of a frequency-grid, a periodic filter is the best solution. A simple Mach-Zehnder (MZ) structure has a periodic transfer function over wavelength, and because wavelength and frequency are almost proportional for these small differences compared to the absolute wavelengths (1530 - 1561 nm), it is a suitable device for the separation of a frequency-couple. For every couple, the channel with the lowest frequency is transmitted to the upper output of the MZ, where it will be modulated, while the channel with the highest frequency is transmitted to the lower output, to be detected. Optical modulation is performed by modulating the drive current of a Semiconductor Optical Amplifier (SOA). The optical signal will be amplified meanwhile. The back facet of the SOA has a high reflectivity, so the modulated optical signal is reflected. After reflection, the signal travels through the SOA in the opposite direction, undergoing the modulation and gain of the SOA again. After the SOA, the signal uses the exact same path while travelling upstream. A schematic overview of the ONU is presented in figure 1.3

If the user wants to receive multiple services, for example a broadcast tv signal and internet on the same time, it is possible that he has to receive two (or even more) downstream wavelengths. in that case, a Coarse Wavelength Demultiplexer has to be placed in front of the ONU. This module can rely on the same technique as used in the wavelength-router, but also other techniques will be considered. A second possible solution can be to use an AWG to separate multiple wavelengths (figure 1.4). In that case, the used channels have to be chosen carefully, to prevent multiple channels to be demultiplexed to the same detector or modulator.

1.2 Assignment of the Graduation Project

The project described in the previous section has a few innovative solutions, considering the electro-optical components. As announced earlier, one of them is part of the ONU design and this is also the basis for this graduation project. Modulation an SOA (reflective or travelling-wave) by drive current has already been reported several times [4–13], but in most cases under different conditions. Extra investigation on the modulation of reflective SOAs, taking into account the requirements deducted from the network design would be advantageous. It is also unclear whether the requirements on amplification and transmission speed, stated in deliverable 1.2 can be obtained. The actual assignment for this trainee-ship is to investigate if modulation of an SOA by drive-current is possible, meeting the requirements deducted from the BBPhotonics project.

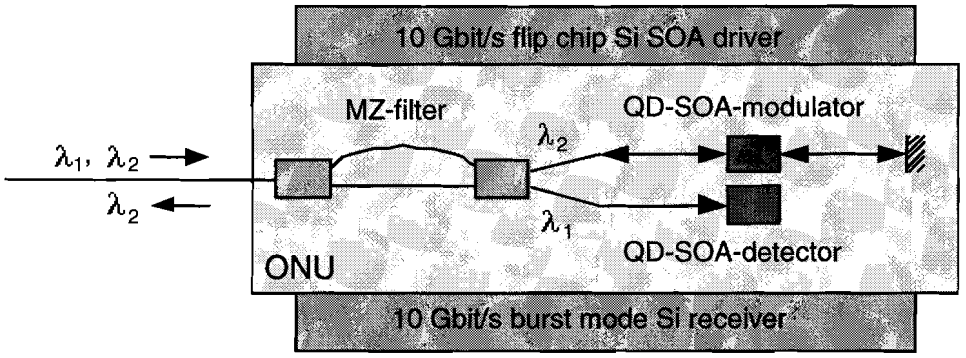

Figure 1.3: Schematic layout of the Optical Network Unit architecture.

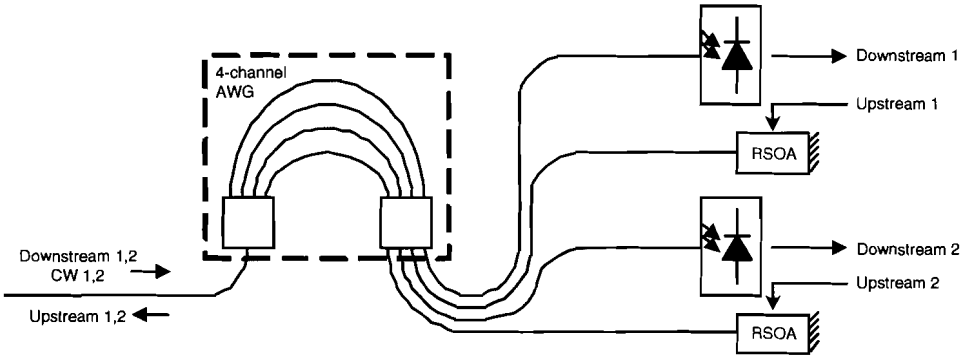

Figure 1.4: Alternative layout of the ONU for reception of two pairs of channels.

This investigation must consists of a part where modulation of an SOA is simulated. This gives insight in the influence of some material parameters that are important for modulation. It can lead to optimum values for some parameters, and it will give a reference to compare the measurements with. Off course, also measurements have to be done. For the measurements, commercially available components will be used, which are probably not designed for this application. Although the eventual system will have a better performance, these measurements can give a good indication whether the required performance can be obtained.

1.2.1 Boundary Conditions

At project meetings it was recognised that the performance requirements on the wavelength router and the amplifiers are quite severe, so it has been decided to relax these requirements. The reference network remains valid, but a target network for first implementation is designed, which has relaxed requirements. This reduces functionality of the network, but also reduces the gap with today's FTTH systems and therefore can be implemented in an earlier stage. Deliverable 1.3 [14] describes the requirements for the new target network:

- Delivery of two wavelength channels per home (one for downstream, one for upstream)
- 1 GbE capacity per wavelength channel
- 16 wavelength channels in the C-band
- 4 remote nodes
- 16 homes per remote node

- maximum fibre length from OLT to first remote node is 20 km
- maximum fibre length between neighbouring nodes is 1 km
- maximum fibre length between remote node and ONU is 5 km
- embedded control signal in 1310 nm wavelength band
- switch at OLT to control network redundancy

These network requirements and a power budget analysis performed for this network lead to some requirements for the reflective SOA. Minimum input power levels and amplification are most important parameters, but also requirements on achievable BER and OSNR are stated [14].

- Received power at RSOA under normal conditions is at least -14.1 dBm
- Minimum RSOA amplification, including modulation loss should be at least 13.1 dB, for the lowest possible received power at the input, the gain will not have to exceed 20 dB
- The extinction ratio of the modulated signal should be at least 12 dB
- The Optical Signal to Noise Ratio of the modulated signal should be at least 35 dB
- For power dissipation reasons, the drive current should not exceed 100 mA

Chapter 2

Review of Semiconductor Optical Amplifier Theory

In this chapter some basic elements of the operation of a Semiconductor Optical Amplifier (SOA) will be explained. Some parameters which are important for the application of an SOA as a reflective amplifier modulator will be treated in more detail.

2.1 Photon-Electron Interaction

Some semiconductor material structures can transform electrical current into light and vice versa. For this process to be possible, some requirements have to be fulfilled. The semiconductor material composition has to have a direct bandgap, the top of the valence band must have the same k-value as the bottom of the conduction band. This is for instance the case with GaAs and InP, while pure Si and Ge have an indirect bandgap. Furthermore, the material has to be designed as a diode structure. This diode structure allows electrons and holes to concentrate at the pn-junction, where they can recombine. An even more efficient structure, called a double heterostructure, is obtained when a very small intrinsic layer with a lower bandgap is placed between the p and n layers. The leakage of electrons and holes is much lower in this case, because they are "trapped" in the intrinsic layer. Recombination mainly takes place in the intrinsic layer, which explains why it is also called the active region. When the electron-hole pairs recombine, the recombination process results in the formation of a photon with energy equal to the energy difference between the original electron and hole, also called the bandgap energy (E_g). The energy of a photon is related to its frequency ν or wavelength λ according to the following relation (h is Planck's constant, c is the speed of light).

$$E_{ph} = h\nu = \frac{hc}{\lambda} \tag{2.1}$$

In reality more processes happen inside the active region of a SOA, where a photon and electron exchange energy. They will be described more detailed afterwards. For a consistent description of these processes and the rate-equations following from it, it is necessary to introduce some parameters. For further simplification, the semiconductor material will be represented by a two-level system, with one energy level as the valence band and one energy level as the conduction band. Without further explanation the following parameters are introduced:

Symbol	Description
f_c	Probability to find an electron in the conduction band
f_v	Probability to find a hole in the valence band
ρ_ν	Density of photons with energy larger than E_g

2.1.1 Radiative Recombination

A photon which enters the active region and has energy larger than the bandgap energy can be absorbed by the semiconductor material. The photon energy is transferred to an electron in the valence band, which is excited and jumps to the conduction band (figure 2.1(a)), an electron-hole pair is created. Since this process involves a photon, an electron in the valence band and an empty space in the conduction band, it is straightforward to describe the stimulated absorbtion rate for this process with the following equation

$$R_a = B_{12}(1 - f_c)(1 - f_v)\rho_\nu \tag{2.2}$$

In this formula B_{12} is the transition probability for this process, $1 - f_c$ and $1 - f_v$ are the probability of an empty space in the conduction band and an electron in the valence band respectively.

An excited electron can also spontaneously recombine with a hole. Its excess energy will be converted into a photon which is emitted, having a random phase and direction (figure 2.1(b)). Looking at the particles this process involves it is straightforward to describe the spontaneous emission rate as follows:

$$R_{sp} = A_{21} f_c f_v \tag{2.3}$$

The electron-hole recombination can also be triggered by an incoming photon. The incoming photon induces the electron-hole recombination, which generates a new photon (figure 2.1(c)). This new photon is an exact copy of the incoming photon, so the direction, frequency and phase of the new photon are equal to that of the incoming photon. The stimulated emission rate can be described with the next formula.

$$R_e = B_{21} f_c f_v \rho_\nu \tag{2.4}$$

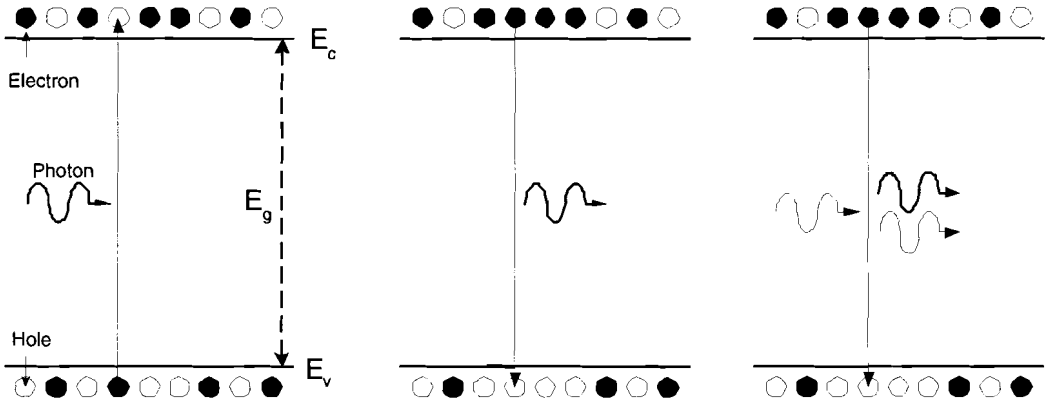

(a) Stimulated Absorbtion (b) Spontaneous Emission (c) Stimulated Emission

Figure 2.1: Three possible radiative recombination processes shown schematically.

2.1.2 Optical Gain

For the purpose of signal amplification, stimulated emission is the most important process in the gain medium of a SOA. From quantum mechanical considerations it follows that the transition probability for stimulated emission is equal to the transition possibility for the absorbtion process, reflected in the Einstein Relations [15]. Thus, coefficients B_{12} and B_{21} are equal and one of them can be replaced by the other. The net stimulated emission rate equals the difference between the stimulated emission rate and the stimulated absorbtion rate. Using Eqs. 2.4 and 2.2 the following relation can be obtained, where ρ_ν is still the density of photons with high enough energy.

$$\begin{aligned} R_{st} = R_e - R_a &= B_{21} f_c f_v \rho_\nu - B_{12}(1 - f_c)(1 - f_v)\rho_\nu \\ &= B_{21}\rho_\nu(f_c + f_v - 1) \end{aligned} \tag{2.5}$$

R_{st} is positive when the emission rate is larger than the absorbtion rate, so when absorption and emission rates are equal, the net stimulated emission is zero and the material is transparent. From Eq. 2.5 the transparency condition can be derived.

$$f_c + f_v = 1 \tag{2.6}$$

At this moment it is useful to replace the parameters f_c and f_v by parameters which are easier to understand. The probability to find an electron in the conduction band, f_c, is clearly proportional to the number of electrons in the conduction band n. Likewise, f_v is proportional to the number of holes in the valence band p. Because the active region of the devices analysed here are all intrinsic and because they need to be neutral of charge, n and p are equal, so they are directly replaced by a general number of carriers, represented by the carrier-density N. Taking the previous consideration into account, Eq. 2.5 is rewritten as:

$$R_{st} = B'_{21}(N - N_0)\rho_\nu \tag{2.7}$$

In this equation, B'_{21} is the new transition possibility and N_0 is the transparency carrier density. The number of generated photons per unit distance (optical gain) is related with the net stimulated emission rate via the group velocity v_g.

$$\frac{d\rho_\nu}{dz} = g = \frac{R_{st}}{v_g \rho_\nu} = \frac{n_{eff} R_{st}}{c\rho_\nu} \tag{2.8}$$

As the net stimulated emission rate is linear with the carrier-density, the gain can be described equally. In that case a is the differential gain, $\partial g / \partial N$.

$$g = a(N - N_0) \tag{2.9}$$

The linearity of the gain can also be deducted from curves calculated with a far more sophisticated model of stimulated absorbtion and emission [16].

For the spontaneous emission rate, Eq. 2.3, the probabilities f_c and f_v can also be replaced by the carrier-density. With this substitution, parameter A_{21} changes into the bimolecular recombination coefficient B.

$$R_{sp} = A_{21} f_c f_v = BN^2 \tag{2.10}$$

2.1.3 Non-Radiative Recombination

Besides the above-mentioned radiative recombination processes, the carrier-density in a semiconductor is also affected by a few non-radiative recombination processes. They can be separated roughly in two classes, linear recombination processes and Auger recombination processes. Linear recombination processes involve only one electron, which can recombine via defects in the semiconductor. Defects can be formed during epitaxy processes, or by absorbtion of impurities at the surface of a semiconductor. These defects generate an intermediate energy state in the bandgap. Electrons from the conduction band recombine via these defects, the energy difference for these transitions is mostly emitted in the form or lattice vibrations (phonons). The recombination rate following from this transition depends only on the number of electrons, represented in the carrier-density N.

$$R_{lin} = A_{lin} N \tag{2.11}$$

The linear recombination coefficient in this formula A_{lin} depends among others on the capture cross section of the trap and the density of traps.

The second important non-radiative recombination process is the Auger process. For this process several variations exist [17]. In the dominant Auger process the energy released during electron-hole recombination is transferred to another electron in the conduction band. The electron

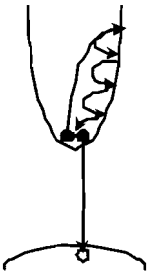

Figure 2.2: Schematic overview of the dominant Auger recombination process.

gets excited to a high energy state, where it relaxes to its original state by emission of phonons (figure 2.2). Since this process involves three carriers (one hole and two electrons) the Auger recombination rate is proportional to the third power of the carrier-density.

$$R_{aug} = C_{aug}N^3 \tag{2.12}$$

Merging the equations for the these processes gives one equation describing the recombination rate due to non-radiative recombination processes.

$$R_{nr} = A_{lin}N + C_{aug}N^3 \tag{2.13}$$

2.2 The Rate-Equations

The most important recombination processes in the active region of an SOA have been described in the previous paragraph. The description of the behaviour of an SOA with respect to optical signals, which will be shown below is originally a description for a laser. In section 2.4 is explained why it is allowed to use this description for an SOA as well. The behaviour of the SOA can be described by two equations, called the rate-equations. One equation describes the change in carrier-density N, while the other equation describes the change in photon-density S.

2.2.1 Carrier-Density Equation

The equation for carrier-density is actually a sum of the influence of all processes that change the carrier-density. The carrier-density is increased by the pump current and decreased by several recombination mechanisms.

$$\frac{dN}{dt} = \frac{\eta_i I}{qV_{act}} - R_{recomb} \tag{2.14}$$

R_{recomb} represents all recombination mechanisms and the first term represents the influence of the pump current I, reduced by the injection current efficiency η_i. q is the electron charge and V_{act} is the volume of the active region. The general recombination coefficient from Eq. 2.14 can be separated in a part representing the net stimulated emission rate of the semiconductor material and a part representing the spontaneous emission and the non-radiative recombination (Eqs. 2.10 and 2.13). For the stimulated emission rate, Eq. 2.9 is substituted in in Eq. 2.8.

$$R_{recomb} = v_g a(N - N_0)\frac{S}{1 + \varepsilon S} + (A_{lin}N + BN^2 + C_{aug}N^3) \tag{2.15}$$

The parameter ε is called the nonlinear gain coefficient, it represents the gain degradation under high pumping conditions. $A_{lin}N + BN^2 + C_{aug}N^3$ can be seen as a loss term and is sometimes represented by N/τ_n with for the carrier lifetime

$$\tau_n = \frac{1}{A_{lin} + BN + C_{aug}N^2} \tag{2.16}$$

Substitution of Eq. 2.15 in Eq. 2.14 gives the final version of the rate equation for carrier density.

$$\frac{dN}{dt} = \frac{\eta_I I}{qV_{act}} - v_g a(N - N_0)\frac{S}{1+\varepsilon S} - (A_{lin}N + BN^2 + C_{aug}N^3) \tag{2.17}$$

2.2.2 Photon-Density Equation

To describe the change in photon-density a comparable equation can be used as for the carrier-density. Because here the perspective of an SOA is used, for the photon-density only photons coherent with the incoming photons are considered. If a laser would have to be described, only photons belonging to the dominant mode(s) are considered. This means that besides the photons from the injected optical power, only photons generated by stimulated emission plus a fraction of the photons generated by spontaneous emission, which is by coincidence coherent with the incoming photons, are taken into account. The injected photon density is processed in the boundary conditions, in the starting value for photondensity. The boundary conditions are not treated here.

$$\frac{dS}{dt} = \Gamma v_g a(N - N_0)\frac{S}{1+\varepsilon S} - \Gamma\beta_{sp}BN^2 - \frac{S}{\tau_p} \tag{2.18}$$

If the first term in the right part of this equation is compared with the second term in the right part of Eq. 2.17, the only difference is the optical confinement factor Γ. This is originated by the fact that the cavity volume occupied by photons V_p is usually larger than the active region volume occupied by electrons, V. The confinement factor Γ represents the electron-photon overlap V/V_p. β_{sp} is the spontaneous emission coupling coefficient, representing the fraction of spontaneous emitted photons coupled into the amplified mode. Several loss mechanisms in the active region are introduced in the rate equation via the photon lifetime τ_p, Examples of these losses are cladding loss, scattering loss and mirror loss. These losses are sometimes joined in a background loss parameter α_i, which is related to τ_p as follows:

$$\tau_p = \frac{1}{v_g\alpha_i} = \frac{n_{eff}}{c\alpha_i} = \frac{n_{eff}}{c(\alpha_{i0} + \alpha_M)} \tag{2.19}$$

Where v_g is the group velocity and n_{eff} is the effective group refractive index. α_{i0} and α_M respectively represent the cavity and mirror losses. The rate equation for photon density is explained above, but it can also be derived directly from Maxwell's wave-equations when some simplifications are applied [16].

2.2.3 Multiple Quantum Well Semiconductors

The description above accounts for bulk active material. If the active region is Multiple Quantum Well (MQW) material some minor changes have to be applied to the rate equations (2.17 and 2.18). The reason why can be seen in figure 2.3. In bulk material, the drive current is directly injected in the active region, while for MQW material, the drive current generates carriers in the Separate Confinement Heterostructure (SCH) which have to be captured in the quantum wells. Carriers can also escape from the quantum wells, returning to the SCH region [18].

The capture and escape processes are described in the rate equations via two timeconstants, τ_{cap} and τ_{esc} respectively. To give a good description of the carrier-density in a MQW semiconductor, the equation for carrier-density is split into one equation for the carrier-density in the SCH region and one equation for the carrier-density in the MQW (active) region.

$$\frac{dN_{SCH}}{dt} = \frac{\eta_I I}{qV_{SCH}} - \left(\frac{N_{SCH}}{\tau_{cap}}\right) + \left(\frac{N_{MQW}}{\tau_{esc}}\right)\left(\frac{d_{MQW}}{d_{SCH}}\right) \tag{2.20}$$

$$\begin{aligned}\frac{dN_{MQW}}{dt} &= \left(\frac{N_{SCH}}{\tau_{cap}}\right)\left(\frac{d_{SCH}}{d_{MQW}}\right) - \left(\frac{N_{MQW}}{\tau_{esc}}\right) - v_g a(N_{MQW} - N_0)\frac{S}{(1+\varepsilon S)} \\ &\quad - (A_{lin}N_{MQW} + BN_{MQW}^2 + C_{aug}N_{MQW}^3)\end{aligned} \tag{2.21}$$

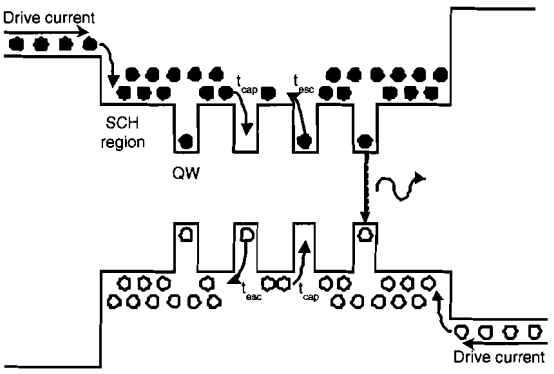

Figure 2.3: Schematic representation of a MQW active region, showing the effects of drive current, capturing and escaping of carriers and recombination.

In Eq. 2.20 the carriers escaped from the quantum well are scaled with the difference in volume of both layers to obtain the increase in carrier density in the SCH layer. This is also done in Eq. 2.21 for the captured carriers. In Eq. 2.20 no recombination term is shown, because the bandgap of this layer is much higher than for the MQW region. Thus, the recombination probability in the SCH layer is much lower than in the MQW region, so it can be neglected in Eq. 2.20. From equation 2.18 the new equation for photon-density can be derived.

$$\frac{dS}{dt} = \Gamma_{MQW} v_g a (N_{MQW} - N_0) \frac{S}{(1+\varepsilon S)} + \Gamma \beta_{sp} B N_{MQW}^2 - \frac{S}{\tau_p} \tag{2.22}$$

2.3 Dynamics of the RSOA module

Limitation of the modulation bandwidth of a RSOA is caused by several phenomena. They will be discussed briefly in this section.

2.3.1 Cavity Travel Time

The optical signal needs time to travel through the cavity. Suppose an instantaneous change in gain at t_0 is applied to an amplifier with a continuous optical input power. The output signal will reach its steady state output power when the photons that entered the amplifier at t_0 exit the amplifier (at $t_0 + \Delta t$). All photons exiting the amplifier before $t_0 + \Delta t$ will undergo the new gain for a shorter time (or length), so the output power before $t_0 + \Delta t$ will be smaller. After $t_0 + \Delta t$ the output power will be stable.
The Δt defined here causes an unavoidable delay between modulation input and optical output power, thus a rise-time and fall-time. The value of Δt depends on the effective refractive index n_{eff} and the lightpath length ΔL.

$$\Delta t = \frac{\Delta L}{v_g} = \frac{n_{eff} \Delta L}{c} \tag{2.23}$$

To give an idea about the influence of this phenomenon, the cavity travel time is calculated for estimated values of effective refractive index and lightpath lengt. n is estimated to be 3.7, the cavity length will be around 700 μm, so $\Delta L = 1.4 * 10^{-3}$ m. For these values, the cavity travel time becomes 17.3 ps. With a modulation speed of 1.25 Gbit/s this is 2.16% of the bitperiod, while for 10 Gbit/s modulation speed it is 17.3% of the bitperiod. In the latter case this phenomena will cause a serious decrease in signal quality.

2.3.2 Parasitic Capacitance

For the modulation of the RSOA, the device gain is changed by changing the drive current. When changing the drive current the device parasitic capacitance limits the achievable modulation speed. The parasitic capacitance is located between the active layer (top) contact and the substrate contact of the device. Because of large uncertainties of parameters defining the capacitance, an exact calculation will not be provided. However, it is useful to present the parameters and the dependence of the capacitance on these parameters. The similarities between this case and the case of a parallel plate capacitor are large, so the parasitic capacitance of the RSOA depends on the same parameters, in the same way. To decrease the parasitic capacitance, the area of the active layer contact can be decreased or the distance between the two plates, mostly dominated by the substrate thickness, can be enlarged. The material permittivity is directly linked with the refractive index, so changing the permittivity is not favourable.
A commercially available Reflective SOA showed an electric 3 dB-bandwidth of 1.8 GHz, which will not lead to severe problems for 1.25 Gbit/s, but for higher bitrates the degradation of the electric signal can cause problems, so attention has to be paid on the electrical design of the RSOA module. The length of the device, which is inherently necessary to obtain high enough gain, is limiting the achievable minimum parasitic capacitance. A more extensive description of the effect of parasitic capacitance, and a possible solution by adjusting the drive current pulseshape is presented in [19].

2.3.3 Modulation Bandwidth as derived for Semiconductor Lasers

Under direct current modulation, the drive current is time dependent and written as

$$I(t) = I_b + I_m(t) \tag{2.24}$$

The response is also considered to of two parts, the first part related to the bias current I_b and a second part containing the response on the modulation current $I_m(t)$. The steady state levels, depending on I_b are called S, N, and the phase ϕ. The modulation current introduces deviations $\delta S(t)$, $\delta N(t)$ and $\delta\phi(t)$ which vary periodically at modulation frequency ω_m. A small signal analysis is presented using a linearised form of the rate equations. This small signal analysis is valid as long as the deviation from the steady state remains small. A general criterium therefore is expressed using the modulation depth.

$$m = \frac{(\delta P)_{max}}{P} = \frac{[I_m(t)]_{max}}{I_b} \tag{2.25}$$

For the validity of the linear approximation, the modulation depth should be smaller than one. The linearised forms of the rate equations for δP, δN and $\delta\phi$ are: [16]

$$\delta\dot{P} = -\Gamma_P \delta P + (G_N P)\delta N \tag{2.26}$$

$$\delta\dot{N} = -\Gamma_N \delta N - G\delta P + I_m(t)/q \tag{2.27}$$

$$\delta\dot{\phi} = \tfrac{1}{2}\beta_c G_N \delta N \tag{2.28}$$

In these equations Γ_P and Γ_N are the small signal decay rates for photons and carriers respectively, and $G_N = \partial G/\partial N$. These equations can be solved in the frequency domain, using Fourier analysis. The solutions are

$$\delta\tilde{P}(\omega) = \frac{G_n P \tilde{I}_m(\omega)/q}{(\Omega_R + \omega - i\Gamma_R)(\Omega_R - \omega + i\Gamma_R)} \tag{2.29}$$

$$\delta\tilde{N}(\omega) = \frac{(\Gamma - P + i\omega)(\tilde{I}_m(\omega)/q)}{(\Omega_R + \omega - i\Gamma_R)(\Omega_R - \omega + i\Gamma_R)} \tag{2.30}$$

$$\delta\tilde{\phi}(\omega) = \frac{\beta_c}{2i\omega}[G_N \delta\tilde{N}(\omega)] \tag{2.31}$$

where

$$\tilde{I}_m(\omega) = \int_{-\infty}^{\infty} I_m(t) \exp(-i\omega t) dt \tag{2.32}$$

The relaxation oscillation frequency Ω_R and relaxation oscillation decay rate Γ_R are given by

$$\Gamma_R = \frac{1}{2}(\Gamma_N + \Gamma_P) \tag{2.33}$$

$$\Omega_R \cong (GG_N P)^{1/2} \tag{2.34}$$

If a sinusoidal modulation is used, where the modulation current is described as follows

$$I_m(t) = I_P \sin(\omega_m t) \tag{2.35}$$

the Fourier transform (Eq. 2.32) of this current is

$$\tilde{I}_m(\omega) = -i\pi I_P[\delta(\omega - \omega_m) - \delta(\omega + \omega_m)] \tag{2.36}$$

where I_P is the peak value of the modulation current and the modulation frequency $\nu_m = \omega_m/2\pi$. Substituting this result in Eq. 2.29 and taking the inverse Fourier transform, the modulated power becomes

$$\delta P(t) = \delta P_0 \sin(\omega_m t + \theta_P) \tag{2.37}$$

where

$$\delta P_0 = \frac{G_N P I_P/q}{[(\omega_m^2 - \Omega_B^2 - \Gamma_R^2)^2 + 4\omega_m^2 \Gamma_R^2]^{1/2}} \tag{2.38}$$

$$\theta_P = \tan^{-1}\left(\frac{2\Gamma_R \omega_m}{\omega_m^2 - \Omega_R^2 - \Gamma_R^2}\right) \tag{2.39}$$

These results show that the modulation response is relatively flat for $\omega_m \ll \Omega_R$, peaks near $\omega_m = \Omega_R$ and drops sharply for $\omega_m > \Omega_R$. The height of the peak around Ω_R depends on the decay rate Γ_R. Because the parasitic capacitance introduces a growing current leakage, measurements hardly show the peak of the modulation response. From analysis of square shaped modulation signals, it appears that for a pulse duration of T, the effective modulation frequency $\nu_m = (2T)^{-1}$, so the amplitude of the response of a sinusoidal modulation current with ν_m is equal to the amplitude of the response on a on-off sequence with bitrate $1/2T$ [16].

2.4 The Simulation Model

In the simulation software a Transmission-Line Laser Model (TLLM) is used to describe the behaviour of a SOA [18]. The idea of a TLLM is based on the algorithm design methods introduced by Johns and Beurle in their Transmission-Line Matrix method of simulating microwave cavities in the time-domain by using meshes of transmission-lines [20, 21]. In a transmission line model, a device is separated in longitudinal sections which are simulated separately [22]. In each section, gain, loss and noise are calculated, after which the results are passed on to the next section via a transmission-line, representing the waveguide propagation delay. In the sections, a laser model is used to calculate the influence of this section on the optical signals, taking all other parameters constant. Of course the internal reflections of in these sections are ignored. The number of sections a SOA is divided in depends on the sampling frequency. Each section is regarded as a spot, which reduces calculation time drastically. The most important assumption taken in the TLLM is that the generated carrier-density by drive current is homogeneous over the entire device length. Using a TLLM for the simulation of active optical components is a very powerful tool, because calculation time is reduced by solving a simple equation for each section, and several TLLM modules can be

cascaded to simulate the great variety of available components nowadays. Polarisation dependence of the optical waveguide is not taken into account in the model.

The parameters used in the simulation model for a bulk SOA, their description and units are given in table 2.1. For the MQW SOA, some parameters are changed. They can be found in table 2.2.

Optical losses due to fiber connection are taken into account via the optical coupling efficiency η_{inj}. In the model, for the background loss α_i which was introduced in Eq. 2.19, a carrier dependent component of the background loss is introduced. The total background loss now can be described as follows.

$$\alpha_i = \alpha_{i0} + N\alpha_{iN} + \alpha_M \tag{2.40}$$

Furthermore, the optical signal gain can be described with a linear model, which is used in all earlier equations, but it can also be described with a logarithmic model. In this case the linear material gain parameter a becomes the logarithmic gain parameter. When the logarithmic model is used (Eq. 2.41b), the chirp is not represented via the linewidth enhancement factor α, but via the differential refractive index dn/dN.

$$g = \Gamma a(N - N_0) \tag{2.41a}$$

$$g = \Gamma a \ln\left(\frac{N}{N_0}\right) \tag{2.41b}$$

In the model, two different ways of calculating the contribution of spontaneous emission to the amplified signal are implemented. The first method, already used in Eq. 2.18, is to determine the contribution of spontaneous emission as a fraction of the total generated spontaneous emission, with the spontaneous emission coupling coefficient β_{sp}. The second method calculates spontaneous emission based on the gain due to stimulated emission, enhanced by the population inversion parameter n_{sp}:

$$S_{sp} = \Gamma\beta_{sp}BN^2 \tag{2.42a}$$

$$S_{sp} = \left(e^{gL} - 1\right) h\nu n_{sp}\frac{g}{g - \alpha_i} \tag{2.42b}$$

Where in Eq. 2.42b the material gain g can be replaced by either of the formulas in Eq. 2.41.

The transition from the bulk model to the MQW model is straightforward. All influenced parameters are split in a component for the separate confinement heterostructure layer and a component for the multiple quantum well layer. The contribution of the SCH layer to the linewidth enhancement is always calculated via the differential refractive index, while for the MQW layer, the way of calculating this contribution depends on if the gain is represented by a linear or logarithmic model.

Symbol	Description	Value	Units
λ	nominal wavelength	1.5525246e-6	m
L	laser chip length	350.0e-6	m
w	active region width	2.5e-6	m
d	active region thickness	0.2e-6	m
Γ	optical confinement factor	0.3	
n_g	group effective index	3.7	
R_l	left facet reflectivity	1.0e-4	
R_r	right facet reflectivity	1.0e-4	
η_{opt}	optical coupling efficiency	1.0	
α_{i0}	fixed internal loss	3000.0	m^{-1}
α_{iN}	carrier dependent internal loss	0.0	m^2
α	material linewidth enhancement factor (used if linear gain)	3.0	
dn/dN	differential refractive index (used if logarithmic gain)	-1.11e-26	m^3
N_{ch0}	chirp reference carrier density	2.0e24	m^{-3}
η_{inj}	current injection efficiency	1.0	
A	linear recombination coefficient	0.0	s^{-1}
B	bimolecular recombination coefficient	1.0e-16	m^3s^{-1}
C	Auger recombination coefficient	1.3e-41	m^6s^{-1}
a	linear material gain coefficient (logarithmic gain if > 1e-10)	3.0e-20	m^2
N_0	transparency carrier density	1.5e24	m^{-3}
ε	nonlinear gain coefficient	1.0e-23	m^3
τ_ε	nonlinear gain timeconstant	0.0	s
f_{st}	offset for gain peak frequency	0.0	Hz
df_{st}/dN	gain peak frequency carrier dependence	0.0	Hz·m^3
δf	gain coefficient spectral width	1.0e15	Hz
$d\delta f/dN$	gain coefficient spectral width carrier dependence	0.0	Hz·m^3
n_{sp} / β	population inversion parameter (spontaneous coupling if < 1)	2.0	
f_{sp}	offset for spontaneous emission peak frequency	0.0	Hz
df_{sp}/dN	spontaneous emission peak frequency carrier dependence	0.0	Hz·m^3
δf_{sp}	spontaneous emission spectral width	1.0e15	Hz
$d\delta f_{sp}/dN$	spontaneous emission spectral width carrier dependence	0.0	Hz·m^3
	initial carrier density	1.0e24	m^{-3}

Table 2.1: Parameters used in the TLLM model for bulk SOAs.

Changed parameters (compared to Bulk model)				
Old Symbol	New Symbol	New Description	Value	Unit
d	d_{MQW}	total MQW active region thickness	0.4e-6	m
Γ	Γ_{MQW}	MQW confinement factor	0.7	
α	α_{MQW}	MQW material linewidth enhancement factor	3.0	
dn/dN	dn_{MQW}/dN	MQW differential refractive index	-1.11e-26	m^3
Added parameters (compared to Bulk model)				
	$d_{HalfSCH}$	one-sided SCH-region thickness	0.21e-6	m
	Γ_{SCH}	SCH confinement factor	0.56	
	dn_{SCH}/dN	SCH differential refractive index (always used)	-1.5e-26	m^3
	τ_{cap}	carrier capture timeconstant	70.0e-12	s
	τ_{esc}	carrier escape timeconstant	140e-12	s

Table 2.2: Changes in parameters for the TLLM model for MQW SOAs.

Chapter 3

Static Simulations

Before starting to measure on an actual amplifier, it is important to know what to expect. Therefore simulations are very useful. For the simulations described, a program specialised in simulation of optical components, circuits and networks is used. The models used by this program to simulate the optical amplifier are already described in section 2.4. The simulated circuit is discussed first, followed by a description of the results from simulations.

3.1 Description of the Simulated Circuit

The main component of the simulated circuit is the optical amplifier, of which the models are described in the preceding section. Using a TLLM model leads to some properties which have to be taken into account. Firstly, a TLLM component can only be simulated if the environment boundary-conditions are set to be aperiodic. This may encounter some difficulties, because boundary-conditions are normally set to periodic and some (spectral) properties of components are only correct when periodic boundary-conditions are applied. On the second hand, any input or output signal of a TLLM component has to consist of (optical or electrical) samples, while the default signal representation is blocks. Some components require blocks as input or output signals, so the signal representation has to be transformed in the circuit. This is chosen to be done right before or after the SOA.

In figure 3.1 different components which together form the simulated system are shown. The SOA has 6 in- and outputs of which 4 are representing bidirectional optical signals transportation (the sides of the device). The input on top of the device is the drive current input and the output on top of the device outputs the carrier density, for measurement purposes. A CW-Laser with a 1 MHz linewidth provides the optical input power of the SOA. Before entering the SOA, this signal is converted from blocks into samples. The drive current is generated by a DC source, which is also converted from blocks into samples. If a Travelling Wave configuration is simulated, like in this case, the left optical input and right optical output are used, while the other optical in- and output are connected to ground. If a reflective SOA is simulated, both optical connections on the right side of the device are used, while both left connections are grounded. The optical output signal is changed from samples to block for easy further processing. The input and output optical power are measured by a powermeter, and the values (in dBm's) are stored in a table, together with the value of drive current which is provided by the "Const"-module. Only the signal amplification is interesting in this case, and not the generated Amplified Spontaneous Emission. Therefore, in the powermeter, the measured bandwidth is reduced to a 3 GHz band around the input frequency. This reduction can be seen as an ideal square-shaped optical filter with a 3 GHz bandwidth.

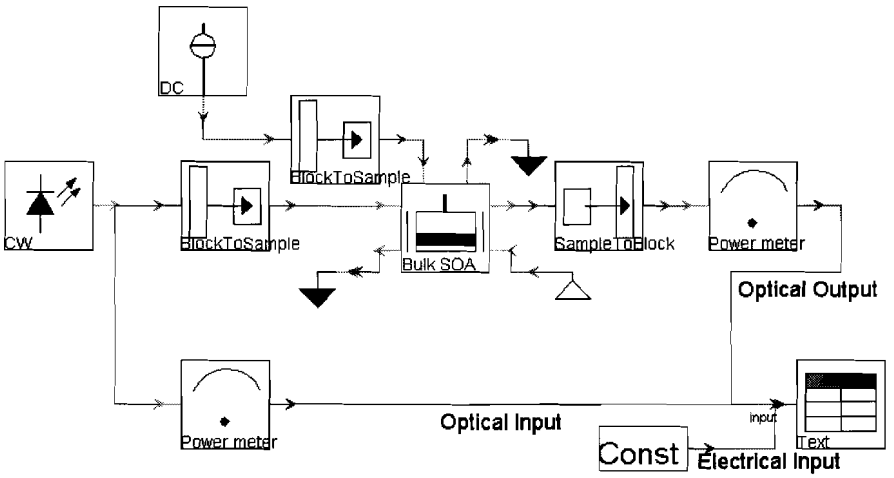

Figure 3.1: The system which is simulated. In this case, the device under simulation is a bulk TW-SOA.

3.2 Results of the Simulations for Bulk Material

In order to obtain most realistic results, parameter values are chosen as much as possible equal to values of the devices which will be measured afterwards. There was only one bulk SOA available for measurement, which could support modulated drive currents. This device had a Travelling Wave configuration, so the SOA had two low-reflective facets. The facet reflectivity is estimated to be 2.0e-5 for each of the facets. The length of the active region of this device is approximately 700 μm. The chip-fiber coupling losses are estimated to be 3 dB, which leads to an optical coupling efficiency of 0.5. Other parameters of the bulk SOA device are not known, so the default values from the model are applied for them. To summarise, for the parameters that have the largest influence on the static characteristics of the SOA, the values used in the simulations are displayed in table 3.1

Symbol	Value	Unit
L	700.0e-6	m
w	2.5e-6	m
d	0.2e-6	m
Γ	0.3	
n_g	3.7	
R_l	2.0e-5	
R_r	2.0e-5	
η_{opt}	0.5	
α_{i0}	3000.0	m^{-1}
η_{inj}	1.0	
a	3.0e-20	m^2
ε	1.0e-23	m^3

Table 3.1: Values for model parameters used in the static simulation of the Bulk SOA.

The simulation program calculated the output power for different values of optical input power, with a sweeping value of drive current. Because the drive current applied to the device under test is limited to 120 mA, the simulated drive current is also limited to 120 mA. The gain current char-

acteristic of this simulated device is shown in figure 3.2. For a drive current of 70, 100 and 120 mA, the saturation characteristic is simulated by sweeping the optical input power. The output saturation characteristic can be seen in figure 3.3.

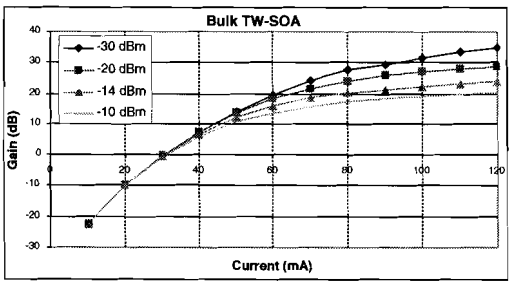

Figure 3.2: Gain-Current characteristic of TW Bulk SOA for different values of input power.

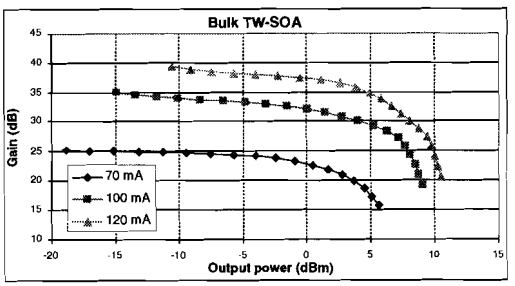

Figure 3.3: Gain as a function of output power for TW Bulk SOA for different values of drive current.

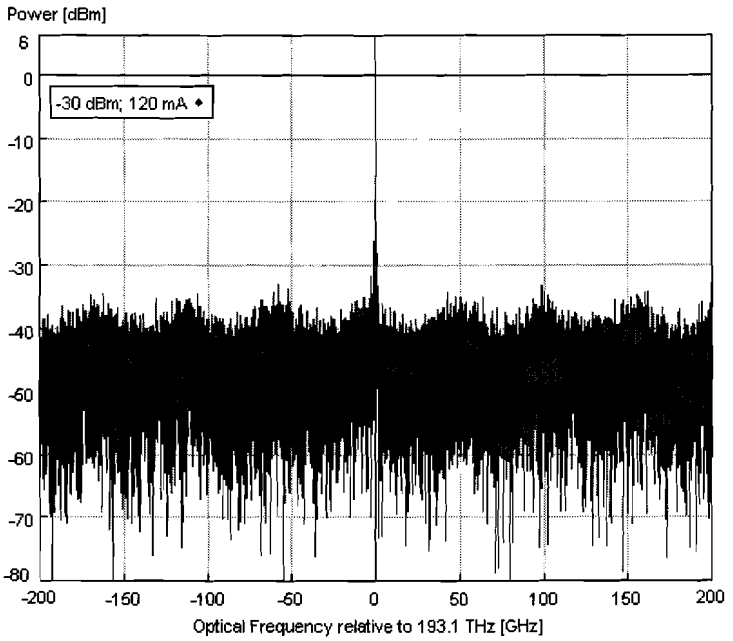

Figure 3.4: Output optical spectrum for low input power and high drive current, cavity resonances can clearly be distinguished.

From figure 3.2 the transparency current can be derived. According to this simulations, the transparency current of the bulk SOA is 30 mA for all input powers. For a gain of 20 dB, which is the maximum value stated in the boundary conditions, drive current has to be at least 60 mA, depending on the optical input power. For an input power of -14 dB, the expected input power, drive current already increases to 80 mA to achieve 20 dB Gain. From figure 3.3 the saturation output power of the simulated Bulk SOA can be determined. This is the output power at which the gain has dropped by 3 dB with respect to the gain for low input power. One would expect the curves to be flat for low input powers. This is not the case because of the measured ASE within the 3GHz bandwidth, which is also taken into account in the calculation of gain. This effect is more prominent for low input power and high drive current. The saturation output powers are 1.25 dBm, 3.5 dBm and 5.25 dBm for 70, 100 and 120 mA drive current respectively.

In figure 3.4 the output spectrum is shown for an input power of -30 dBm and drive current of 120 mA. Cavity resonances are clearly visible in this figure, they are caused by the combination of low input power and high drive current. Because of the low input power, the spontaneous emission rate is relatively high. Even though the reflections at the facets are low, cavity resonances appear for high drive currents. The mode spacing between the cavity resonances is directly related to the cavity length. The phase condition for threshold condition states that after one cavity roundtrip, the phase of the optical signal is equal to the original phase. For two neighbouring modes, this can be deducted to the following simple equation, with $\Delta\nu$ representing the spacing between resonance frequencies of the optical signal, c the velocity of light, L the cavity length and n the refractive index.

$$\Delta\nu = \frac{c}{2Ln} \tag{3.1}$$

From the spectrum shown above, the spacing between resonance frequencies is 53.47 GHz. With the refractive index from table 3.1 the device length calculated from the cavity resonances is 757.5 μm. The difference with the 700 μm which was used in the simulations is caused by the finite value of sample frequency. For a higher sample frequency the length becomes more exact, but simulations take much more time.

3.3 Results of the Simulations for MQW material

For the simulation system of a MQW SOA, the SOA module from figure 3.1 is replaced by a module representing a MQW SOA. Also for this simulation some parameters from the model are changed into values representing the device which eventually will be tested. This device is a commercially available reflective MQW SOA module, with SMA modulation input and integrated input impedance matching. Because this device is reflective, the output power of the SOA is measured from the left device output, while the right output is grounded.

Symbol	Value	Unit
L	525.0e-6	m
w	1.2e-6	m
d_{MQW}	0.056e-6	m
$d_{HalfSCH}$	0.059e-6	m
Γ_{MQW}	0.07	
$\Gamma_{HalfSCH}$	0.56	
n_g	3.7	
R_l	8.0e-6	
R_r	0.3	
η_{opt}	0.5	
α_{i0}	3000.0	m^{-1}
η_{inj}	1.0	
a	5.0e-20	m^2
ε	1.0e-23	m^3
τ_{cap}	70.0e-12	s
τ_{esc}	140.0e-12	s

Table 3.2: Values for model parameters used in the static simulation of the MQW SOA.

The datasheet of the device and two articles about the device layout [23, 24] provided useful information for the parameter values used in the simulations. The reflective SOA has a cleaved

facet as reflective facet, so $R_r = 0.3$. The left facet has a low reflectivity, caused by the use of a tapered, angled active waveguide combined with a passive window region. The left facet reflectivity R_l is estimated to be decreased to 8e-6 due to all these effects. The active waveguide of the device consists of an untapered curved region and a tapered region. Because tapering is not included in the MQW model, the active region is approximated by a square shaped active waveguide with a length equal to the length of the untapered region and half the length of the tapered region. The linear material gain is estimates somewhat higher than for the bulk SOA. Table 3.2 shows some parameter values used in the simulations.

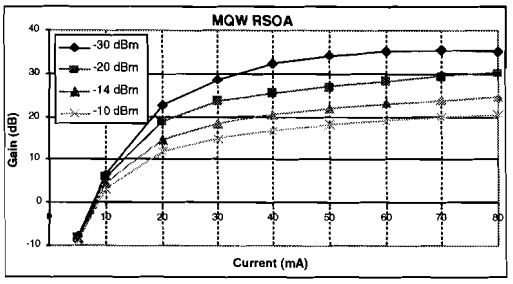

Figure 3.5: Gain-Current characteristic of MQW Reflective SOA for different values of input power.

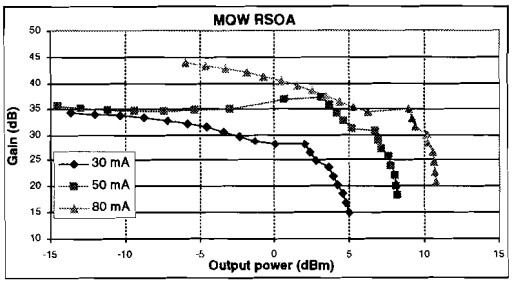

Figure 3.6: Gain as a function of output power for MQW Reflective SOA for different values of drive current.

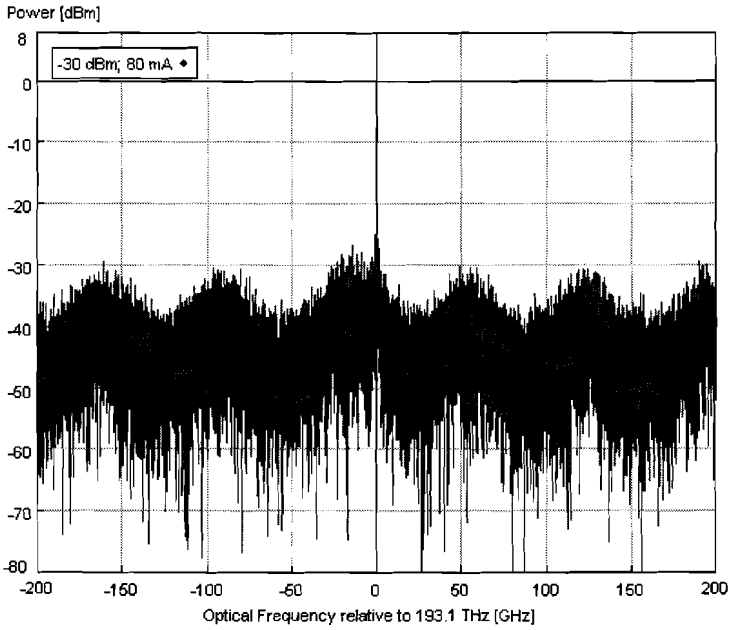

Figure 3.7: Optical spectrum of the output signal of the MQW Reflective SOA, showing cavity resonances.

These values are inserted in the model and equal simulations as for the bulk material are performed. Because the drive current of the real RSOA is limited to 80 mA, the simulations will not use higher drive currents. The results are shown in figures 3.5 and 3.6. From these figures, the transparency drive current is around 8 mA. 20 dB Gain is already obtained at a drive current of 18 dB for low input powers. For -14 dB input power, 20 dB gain is obtained at 40 mA drive current. The saturation characteristic shows unexpected behaviour. The cavity resonances which can be seen in figure 3.7 are much more severe compared to the bulk amplifier. They have large

influence on the saturation characteristics. First of all, the amount of measured ASE in the signal is larger compared to the bulk simulations. Also for changing input power, the refractive index changes, which leads to a shift of the resonance spectrum. This can cause sudden large changes in the saturation characteristics.

For high values of drive current and low inserted optical power, the spectrum of the optical signal shows again cavity resonances. The amplitude of the resonances is larger compared to that for the Bulk SOA, because of the high reflectivity of the right facet. Shorter cavity length leads to smaller mode spacing. Also in this case, the cavity length can be calculated from the resonance spectrum. A mode spacing of 71.2 GHz leads to a cavity length of 569 μm, while the real simulated length is 525 μm. Explanation for this is again the limited sample frequency.

3.4 Comparison of the Simulations of Bulk and MQW devices

If the results of the simulations for the Bulk device are compared with the results of the simulations for the MQW device, a few interesting things can be noted.

- The transparency current for MQW devices is much lower than for Bulk devices. This can be explained by the smaller active area and lower background loss in a MQW device. Because the active area is lower, a lower drive current is needed to obtain equal carrierdensity. A lower gain is necessary to compensate for the lower background loss, which also reduces the transparency current.
- The slope of the MQW device starts steeper, but reduces quickly, compared to the bulk device. This can be explained by the higher linear material gain. Higher gain also leads to saturation at lower drive currents.
- Larger and wider spaced cavity resonances. Different values for reflectivity and different cavity length cause these differences.
- The cavity resonances cause the nonlinearities in the saturation characteristics of the MQW device.

Chapter 4

Static Measurements

In the previous chapter it is already mentioned that two devices were available to be measured, and the model parameters for the simulations are adjusted to match the properties of these devices. In this chapter the static measurements on these devices are discussed, but not after the measurement system is discussed. Because the bulk and MQW device both have a different configuration, they are discussed separately.

4.1 Measurements on the Bulk SOA

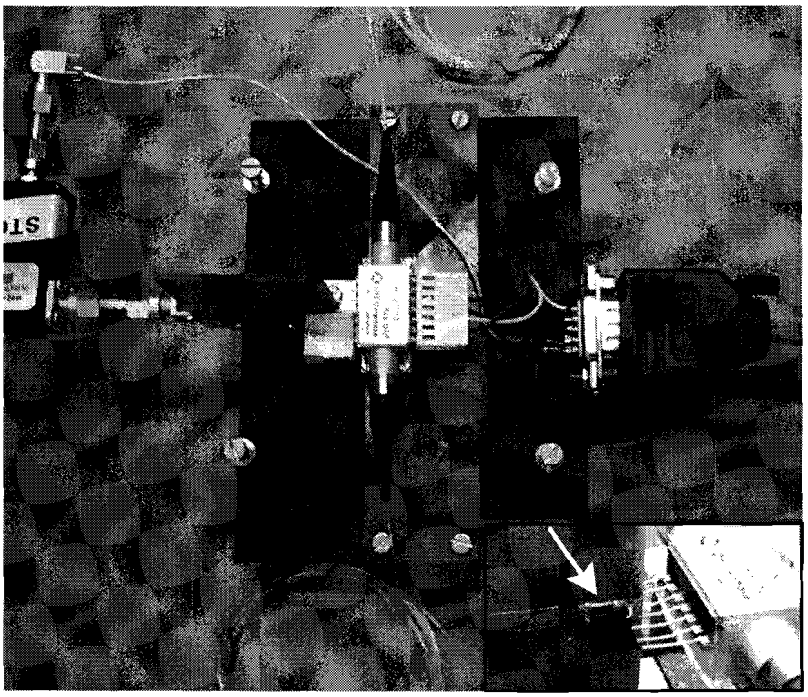

Figure 4.1: Picture of the bulk TW-SOA device. The inset shows the soldered resistors to adjust the input impedance.

The bulk device under test has a Travelling Wave (TW) configuration. It is packaged in a 14-pin butterfly package, so it was originally meant for static applications. If high speed modulation has to be applied, the input impedance and the connectors have to be matched to those of the driving circuit. All available signal generators have a SMA connector with 50Ω output impedance, so

the SOA cathode and anode output with low impedance of the butterfly package have to be transformed to a 50Ω SMA output. This is done by soldering the pins to an etched transmission line on a PCB, with a 50Ω series resistance near the butterfly pins. On the new output, a SMA connector is placed. The result can be seen in figure 4.1. This modification is not strictly necessary for static measurements, but for better correspondence between static and dynamic measurements it is already applied. The applied series resistance introduces large loss in the drive current circuit. The laser controller has a limited output voltage, leading to a maximum DC drive current of 120 mA.

4.1.1 Measurement System for the Bulk TW-SOA

The measurement system and the simulation system are very comparable, the main elements are present in both setups. The CW-laser and the powermeter are even physically present. The Drive current is provided by a Laser Controller module, which also controls and adjusts the temperature of the amplifier. Furthermore, an isolator is applied between the CW-laser and the amplifier to provide signals reflected in the SOA to enter and distort the laser. A polarisation controller is used to find the polarisation state with optimum amplification of the SOA. The output power of the CW-laser cannot be tuned to the low values required for the saturation measurement, so a manual attenuator solves this problem. The linewidth of the CW-laser is 150 kHz. The system is shown in figure 4.2.

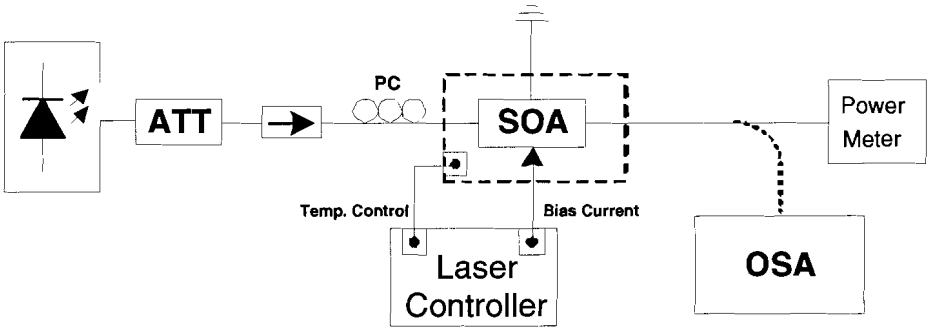

Figure 4.2: Schematic of the measurements system for static measurement on the bulk TW-SOA.

4.1.2 Measurement Results for the Bulk TW-SOA

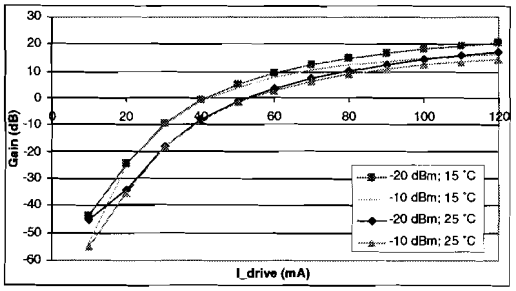

Figure 4.3: Gain-Current characteristic of TW Bulk SOA for different values of input power and temperature.

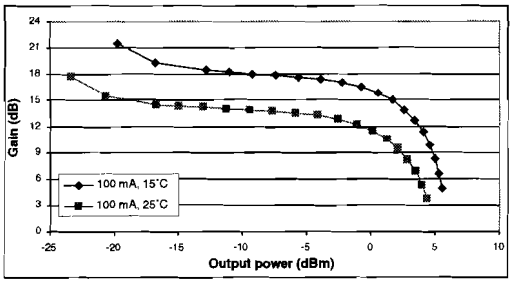

Figure 4.4: Gain as a function of output power for TW Bulk SOA for constant drive current and different temperature.

The measurements are performed equal to the simulations, first with some values for input power and sweeping drive current. Also two different temperatures are applied during measure-

ments. In figure 4.3 the results can be seen. From this graph can be seen that the transparency current is around 45 mA, depending on the temperature.
Because of the high transparency current, the saturation characteristic is only measured for one value of drive current, 100 mA. The result can be seen in figure 4.4 where two values of temperature are evaluated. The measurements for low values of input power are less precise, because filtering is not applied, so the measured ASE is dominating in the measurements. For both temperatures, the output saturation power is around 1 dBm. It is nice to notice that an increase of temperature leads to lower gain, but does not affect the saturation power, thus gain can be controlled by temperature of the device.

4.2 Measurements on the MQW SOA

The MQW device under test is a commercially available Reflective SOA. It has an integrated impedance matching circuit and a SMA connector for the drive current supply. Temperature control is provided via 7 regular connector pins on the other side of the device. The bias current is supplied to the device via a bias-tee, so the modulation current can be superimposed while performing the dynamic measurements. The RSOA with mounting block, bias-tee and fiber pigtail is packaged to protect the vulnerable fiber pigtail. Figure 4.5 shows a photograph of the packaged RSOA module.

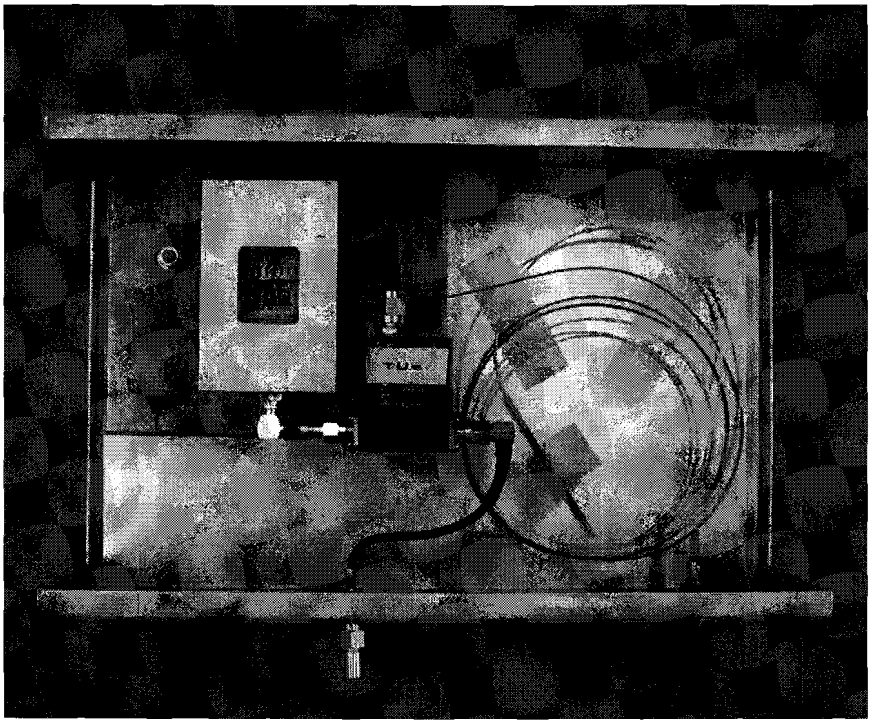

Figure 4.5: Picture of the packaged RSOA, the white connector with the arrow on it provides the temperature management.

4.2.1 Measurement system for the MQW RSOA

Figure 4.6 shows the measurement system for the MQW reflective SOA. Because the reflective SOA has only one fiber pigtail, the input power and output power run through the same fiber. In the static measurement they are separated by a 50/50 coupler. This however introduces 3 dB loss in each direction. The part with the optical source is equal to the setup for the bulk SOA,

using a CW source, isolator and attenuator. The CW-laser in this setup however has a linewidth of 1 MHz. Also a polarisation controller is applied right before the RSOA. The input power is measured from the second output of the coupler, while the second input of the coupler is used to measure the output power. The output power is filtered before being measured, using an optical Band-Pass Filter (BPF) with a bandwidth of 3 nm.

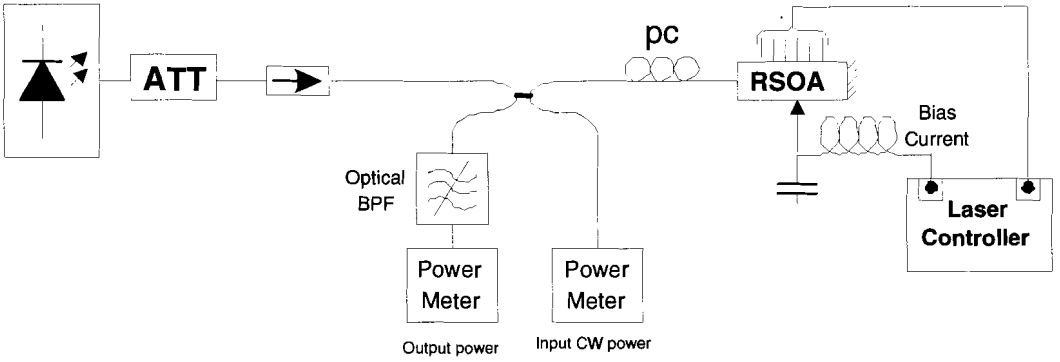

Figure 4.6: Schematic showing the measurement system for the static measurements of the RSOA.

4.2.2 Measurement results for the MQW RSOA

With constant optical input power, the drive current of the RSOA is changed, and the output power is measured. This is performed for different values of optical input power. In this case, the temperature is kept constant at 20°C The results can be seen in figure 4.7. All measurements are done for a polarisation state that gave the highest output power. The transparency current is around 10 mA. Also, for a fixed drive current, the optical input power is varied, see figure 4.8. The obtained graphs show a saturation output power of 1, 5 and 7 dBm for drive current of 30, 50 and 80 mA respectively.

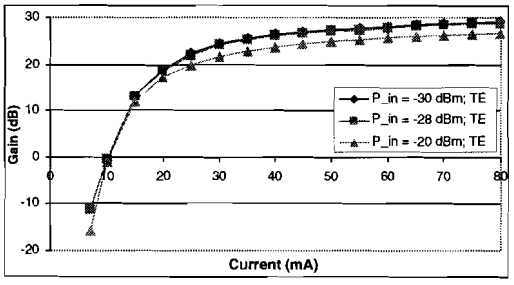

Figure 4.7: Gain-Current characteristic of MQW RSOA for different values of input power.

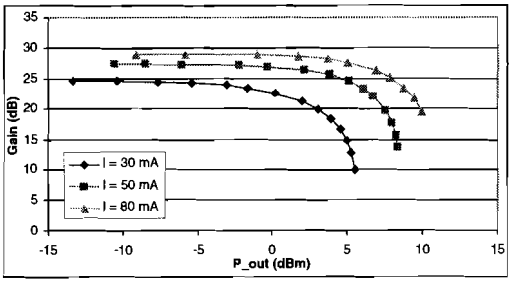

Figure 4.8: Gain as a function of output power for MQW RSOA for constant drive current and different temperature.

Chapter 5

Dynamic Simulations

Comparison of the static simulations with the static measurements show some discrepancies. To improve the quality of the simulations, the results of the static simulations are modified so they will match with the results of the measurements. Therefore some parameters from the model are changed. First this matching is explained and the new parameters are shown. The dynamic simulation circuit and the results are shown afterwards.

5.1 Matching of Simulations with Measurements

5.1.1 Matching for the Bulk TW-SOA

As a reminder, the results of the simulations and measurements are put into one graph, without matching. In figure 5.1 it appears that the measured transparency current is much higher than the simulated transparency current. Also important is the much higher gain achieved in simulations. The difference in simulated gain for both input powers is much larger than for the measurements.

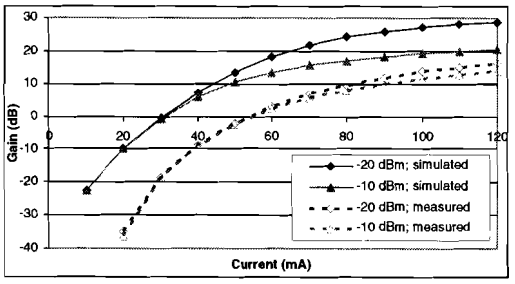

Figure 5.1: Simulated and measured characteristics without parameter matching, dotted lines show the results of the measurements.

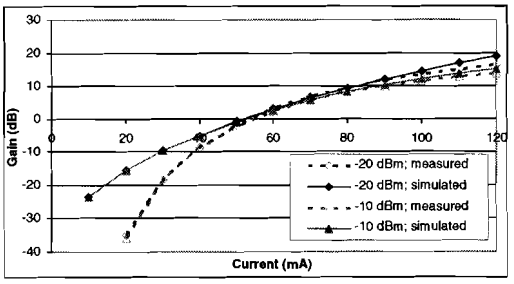

Figure 5.2: Simulated and measured characteristics after parameter matching, dotted lines show the results of the measurements.

These differences have to be reduced to improve the quality of the simulations. Increasing the simulated transparency current can be done by applying a lower gain, a higher background loss or a higher transparency carrier-density. Lowering the gain can be achieved by decreasing the optical confinement coefficient or by decreasing the linear material gain. Adjustments in the cavity dimensions also influence transparency carrier density. Changing the nonlinear gain coefficient influences the curves for higher values of drive current.

By changing these parameters, the simulated curves must become about equal as the measured curves. While trying to achieve this, it appeared to be very difficult. This is caused by the large

number of parameters which can be varied, and the complex influence of these parameters on the behaviour of the optical amplifier. A decision has to be made, whether to aim for a good shape of the curve, but obtained with lower values of currents, or to aim for a partially good match, only for currents above transparency current. The latter possibility was chosen, and the results of the matching can be seen in figure 5.2. The parameter values used for the simulation are shown in table 5.1. From the results of the improved static simulations, the drive currents corresponding with a digital '0' or '1' can be deducted. 50 mA drive current will be applied for a '0' and 120 mA is applied for a '1'.

Symbol	Value	Unit
L	700.0e-6	m
w	2.3e-6	m
d	0.23e-6	m
Γ	0.25	
n_g	3.7	
R_l	2.0e-5	
R_r	2.0e-5	
η_{opt}	0.5	
α_{i0}	4000.0	m^{-1}
η_{inj}	1.0	
a	2.3e-20	m^2
ε	1.0e-22	m^3

Table 5.1: Values for model parameters used in the dynamic simulation of the Bulk SOA.

5.1.2 Matching for the MQW RSOA

For the MQW Reflective SOA, equal actions are taken. Figure 5.3 shows the simulated and measured gain-current relations without any matching. The difference between the simulated and measured graphs is obviously less significant. The largest difference between both curves is the much larger difference in gain for high drive currents, between both values of input power. Also the high cavity resonances limit a correct representation of reality.

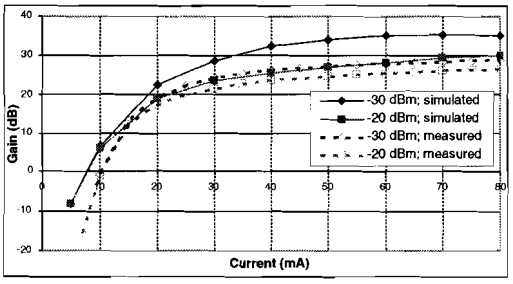

Figure 5.3: Simulated and measured characteristics without parameter matching, dotted lines show the results of the measurements.

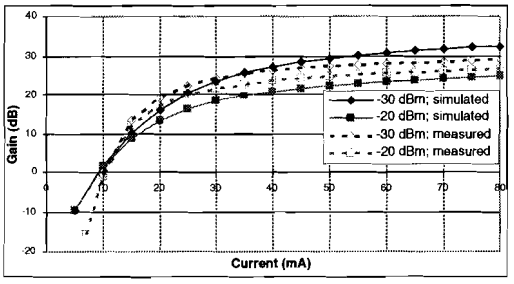

Figure 5.4: Simulated and measured characteristics after parameter matching, dotted lines show the results of the measurements.

Again it appeared to be very difficult to find a set of parameters which gives simulation results equal to the results of the measurements. The best results were obtained with the set of parameters from table 5.2. The curves for these parameter values are shown in figure 5.4. Most interesting adjustment is the reduction of the left facet reflectivity. This is the most straightforward method to reduce the cavity resonances without reducing the gain of the module. The reduced confinement

factor for the SCH-region and the reduced group effective index lead to lower influence of chirp, which will be explained later. The drive currents for this case are 8 mA for a '0' and 40 mA for a '1'.

Symbol	Value	Unit
L	525.0e-6	m
w	1.2e-6	m
d_{MQW}	0.056e-6	m
$d_{HalfSCH}$	0.059e-6	m
Γ_{MQW}	0.055	
$\Gamma_{HalfSCH}$	0.2	
n_g	3.0	
R_l	1e-7	
R_r	0.3	
η_{opt}	0.5	
α_{i0}	2000.0	m^{-1}
η_{inj}	1.0	
a	5.0e-20	m^2
ε	5.0e-21	m^3
τ_{cap}	70.0e-12	s
τ_{esc}	140.0e-12	s

Table 5.2: Values for model parameters used in the dynamic simulation of the MQW RSOA.

5.2 Description of the Dynamic Simulation System

In figure 5.5 the simulation circuit is shown. The left part of the simulation circuit is actually equal as for the static simulations, with the only difference in the provision of drive current. In the dynamic simulations, the drive current is provided by a PRBS-generator, followed by a rectangular shape pulse generator. The bias current and amplitude of this module can be adjusted. At the output of this system two filter modules are added. These modules represent respectively the Mach-Zehnder duplexer in the ONU, and the filter characteristic of the wavelength router. The MZ-filter has a period of 400 GHz and the trapezoid filter has a bandwidth of 18 GHz. After filtering, the signal is detected by a photodiode and it is fed through a low-pass filter. This filter is a second order Bessel filter with a passband of 10 GHz. A clock recovery module and a Bit Error Rate module provide information about the BER of the received signal. Both of these modules need a reference input. The eye-diagram is measured right before the photodiode. While

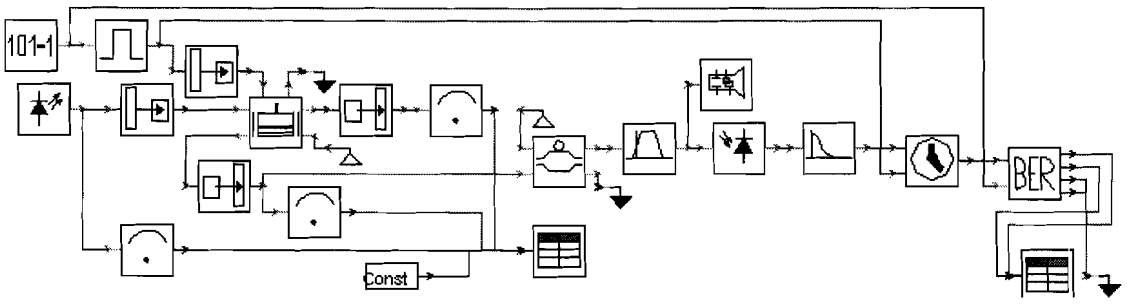

Figure 5.5: Simulation Circuit for the dynamic simulations. In this configuration the SOA is reflective.

describing the static simulation circuit, it was mentioned that some components only work correct if periodic boundary conditions are applied. One of these components is the Mach-Zechnder filter. With aperiodic boundary conditions, like applied here, the delay is quantized to a sample interval, forcing the free-spectral-range to be a sub-multiple of the simulation bandwidth.

5.3 Results of the Dynamic Simulations

5.3.1 Results for the Bulk TW-SOA

The simulations are performed with the model parameters from table 5.1. The eye diagram in figure 5.6 shows the result for 625 Mbit/s bitrate, which is only half of the targeted modulation speed. With an input power of -20 dBm the time-averaged gain, which includes the modulation loss, is 15 dB. The BER of the simulated signal is around 10^{-5}. If the modulation speed is decreased to 500 Mbit/s the detection is almost error-free with a BER of $2 * 10^{-9}$. If the input power is increased to -14 dBm, the BER decreases drastically to $6.4 * 10^{-10}$ for modulation speed of 625 Mbit/s. The eye diagram for this case is shown in figure 5.7. In this case the gain is 13.4 dB.

5.3.2 Results for the MQW RSOA

Also for the MQW RSOA dynamic simulations are performed. For -20 dBm input power and modulation speed of 625 Mbit/s the calculated BER is in the order of 10^{-40} which means perfect error-free reception. The time-averaged gain under these conditions is 15.4 dB. The eye diagram is shown in figure 5.8. The dip in the eye-diagram for the 1-0 transition is caused by chirping. The wavelength of the incoming signal temporarily shifts outside the filter bandwidth, so the received power drops suddenly. If the bitrate is increased to 750 Mbit/s, the BER becomes $3.0 * 10^{-16}$. Increasing the bitrate further, to 1 Gbit/s gives a BER of $2 * 10^{-5}$. If then the input power is increased to -14 dBm, the BER is $6.9 * 10^{-6}$. The amplification in this case is only 8.4 dB. The eye diagram for this case is shown in figure 5.9.

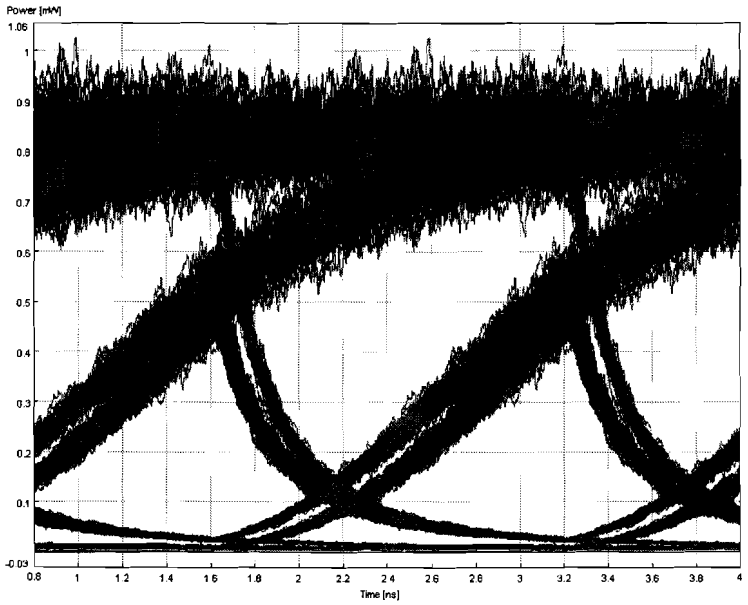

Figure 5.6: Eye diagram of the modulated signal, with a modulation speed of 625 Mbit/s and input power of -20 dBm.

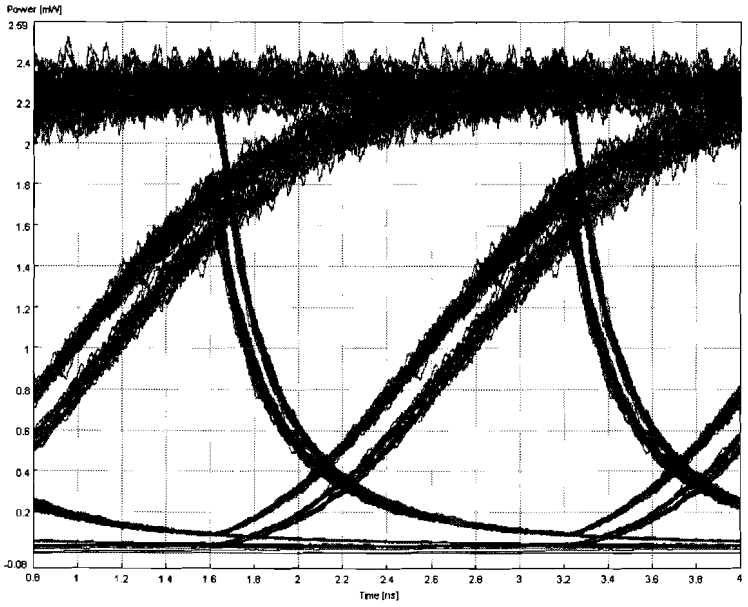

Figure 5.7: Eye diagram of the modulated signal, with modulation speed of 625 Mbit/s and input power of -14 dBm.

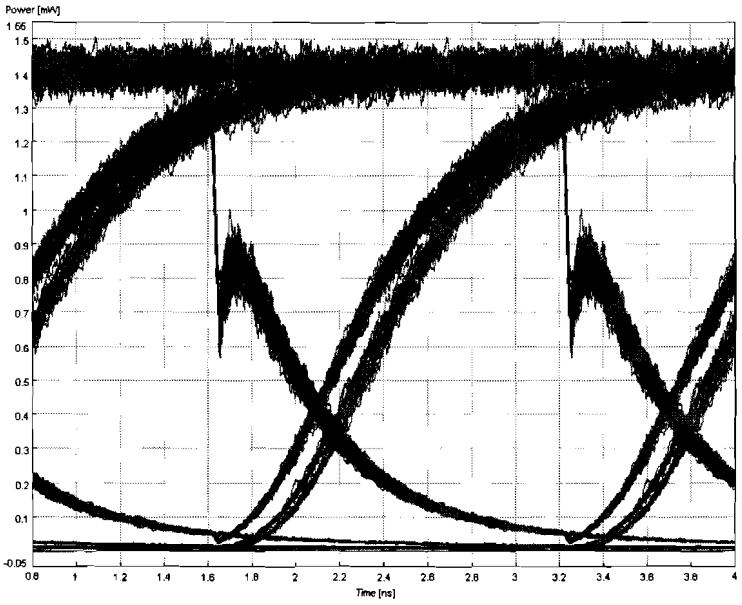

Figure 5.8: Eye diagram of the modulated signal for a modulation speed of 625 Mbit/s and input power of -20 dBm. The dip in the eye is caused by chirping.

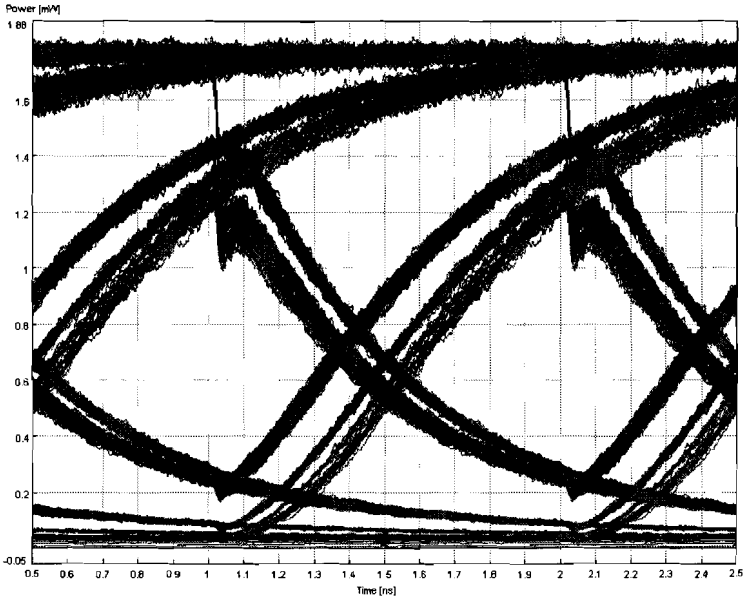

Figure 5.9: Eye diagram of the modulated signal for a modulation speed of 1 Gbit/s and input power of -14 dBm.

Chapter 6

Dynamic Measurements

At last dynamic measurements are performed. These measurements are only performed on the MQW reflective SOA, because this device was specially designed for these purposes, so it will have superior performance to the bulk device, which can also be deducted from the dynamic simulations. In this chapter, first the measurement system is discussed, followed by a description of the results form the measurements. The obtained results are again used to adjust model parameters. This time a realistic representation of the obtained eye-diagram is targeted, so this can be used to predict the behaviour of the complete network with simulations. These simulations are not part of the assignment, and are carried out by a colleague.

6.1 Description of the Measurement System

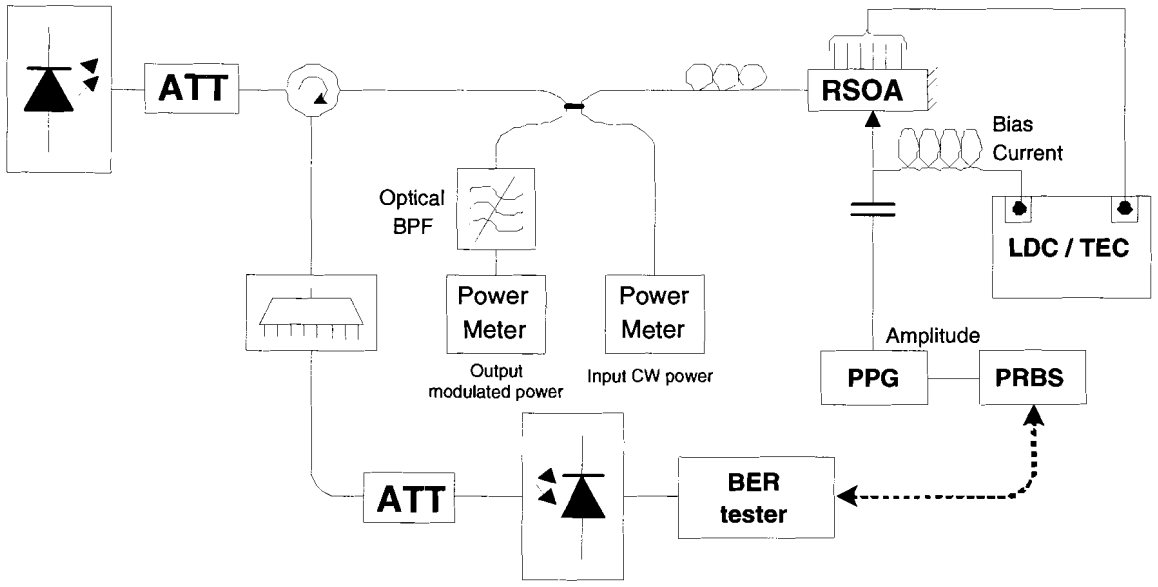

Figure 6.1: Measurement system for the dynamic measurements of the reflective SOA.

The layout of the measurement system is based on the measurement system for the static measurements. In figure 6.1 the system can be seen. A tuneable laser source generates the CW input signal for the RSOA, which can be attenuated first. This signal is fed through a circulator to a 50/50 coupler. The coupler is applied in the system to monitor the input and output power. The monitor of the output power is filtered before it is detected. A polarisation controller is

used to optimise the polarisation of the input CW-signal. This signal is inserted into the RSOA where it is amplified, modulated and reflected. The modulated signal passes the coupler before the circulator separates the signal from the input CW-signal running the opposite direction. A demultiplexer is used to filter the signal like it would happen in the wavelength-router in the eventual system. The bandwidth of this filter is 0.88 nm with a center wavelength of 1552.56 nm, which is about equal to a filter bandwidth of 110 GHz. After the filter an attenuator is placed which will be used to investigate the minimum received power for error-free detection. An HP lightwave converter converts the optical signals into electrical signals, which are detected by a Bit-Error-Rate Tester. The bias current and temperature control are provided from a Laser Diode Controller / TEmperature Controller module. The amplitude is provided by a Pulsed Pattern Generator, driven by a PRBS generator. The output of the PRBS generator is also linked to the BER tester as a reference signal. In this system it is no longer necessary to apply an isolator, because the circulator has high isolation ($\sim$ 60 dB), high directivity ($\sim$ 40 dB) and high return loss ($\sim$ 60 dB). The loss in this system are quite severe. However the pass through loss of the circulator is only 0.7 dB, the total loss of this setup is around 6 dB for the modulated signal and almost 4 dB for the CW-signal. This is mainly caused by the coupler and the insertion loss of the demultiplexer.

6.2 Results of the Dynamic Measurements

6.2.1 Determination of the Achievable Bitrate

The simulation results indicate high bitrates are hard to obtain, so first tests are performed at low bitrate of 500 Mbit/s, to see if the system works. The length of the codeword in these simulations is $2^{31} - 1$. The amplitude of the drive current, provided by the PPG is limited to approximately 40 mA, because the voltage swing of the PPG applied here is limited to 2 Volts. This maximum swing is applied centred around the bias current. From the static measurements on this device, the transparency current appeared to be 10 mA, which is the value corresponding with a digital 0. Thus, the bias current provided by the LDC has to be 30 mA. The input CW signal power is -28 dBm. Under these conditions the eye diagram from figure 6.2 is obtained.

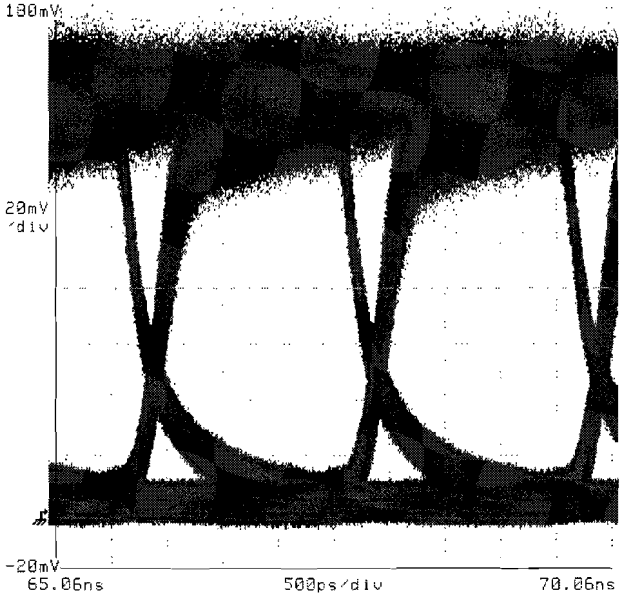

Figure 6.2: Eye diagram for 500 Mbit/s modulation.

The results from the first measurements already promise a lot higher modulation rate. The targeted bitrate of 1.25 Gbit/s is now investigated, with a codeword length of $2^{31} - 1$. It immediately shows good results, and error-free detection is possible. To improve the performance even further, the bias current is adjusted to obtain higher extinction ratio. This will lead to lower necessary received power for error-free detection. These results are discussed in the next section. A '0' current of 8.7 mA and a corresponding '1' current of 47.3 mA gave optimum results for extinction ratio. This means that the '0' current is below transparency current. This is plausible, because the eye diagram from figure 6.2 already shows a slower falling edge than the rising edge. If now the '0' current is decreased, the carrier-density for a '0' drops below transparency, leading to a quicker falling edge, while the rising edge will become slightly slower. This tradeoff has an optimum value for the drive currents given earlier. The eye diagram for this case is shown in figure 6.3. The spectrum shown in figure 6.4 is also for 1.25 Gbit/s modulation speed. In this figure the filtering of ASE can clearly be recognised in the trapezoid shape. The ASE spectrum in the filter passband shows a slightly wavy character, caused by cavity resonances within the RSOA. Also, from this figure the Optical Signal-to-Noise Ratio can be determined, it is over 25 dB.

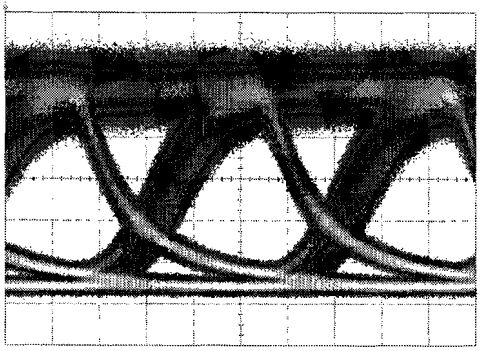

Figure 6.3: Eye diagram for 1.25 Gbit/s modulation with drive currents optimised for maximum extinction ratio.

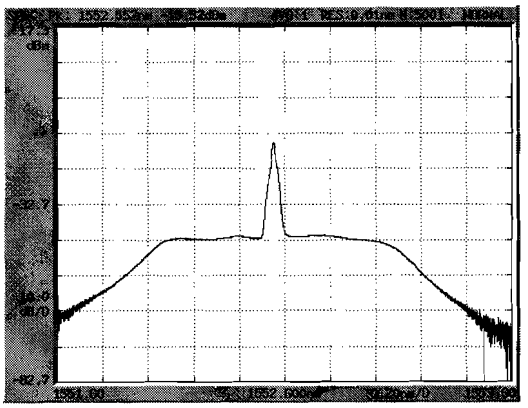

Figure 6.4: Spectrum of the modulated signal. The carrier and the filtering can clearly be distinguished.

If even higher bitrates are applied, pattern effect are growing and are causing errors in the detection. figure 6.5 shows the eye diagram for 2 GBit/s modulation, with bias current of 30 mA. For these measurements a short codeword $(2^7 - 1)$ is used, the input power is still -28 dBm. Now again the bias current is changed, but unlike the previous case, a higher bias current improves the performance of this system. It has to be noted that the extinction ratio in this case is not the most important parameter. Since the highest possible bitrate with error-free reception is investigated, the symmetry of the eye and the eye-opening become indications of performance. For higher bias current, the pattern effect decreases and the crossing of the rising and trailing edge becomes more centered, as can be seen in figure 6.6. The eye-opening increases until a maximum value is reached. After reaching this value, the eye-opening decreases because of larger saturation in the gain-current characteristic. Applying these phenomena, error-free transmission with 2.5 Gbit/s, $2^7 - 1$ bitstream was successfully performed(figure 6.7). If the loss in the measurement system is lower, higher bitrates would even be possible. Also, if a larger current swing than 40 mA can be applied, the achievable bitrate will increase.

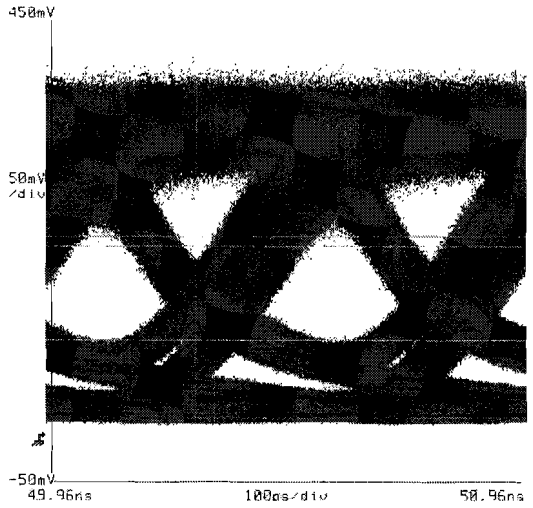

Figure 6.5: Eye diagram for 2 Gbit/s modulation and bias current of 30 mA.

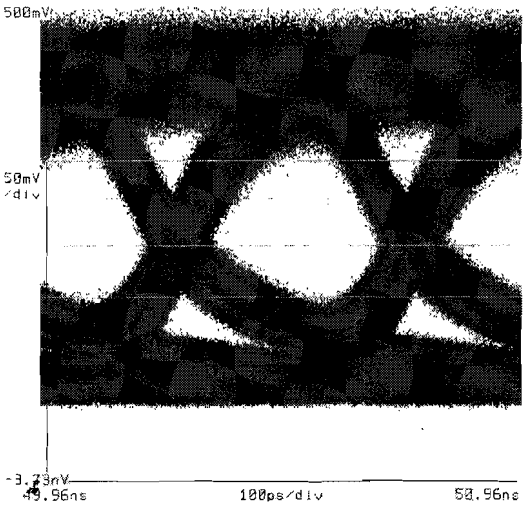

Figure 6.6: Eye diagram for 2 Gbit/s modulation and bias current of 40 mA.

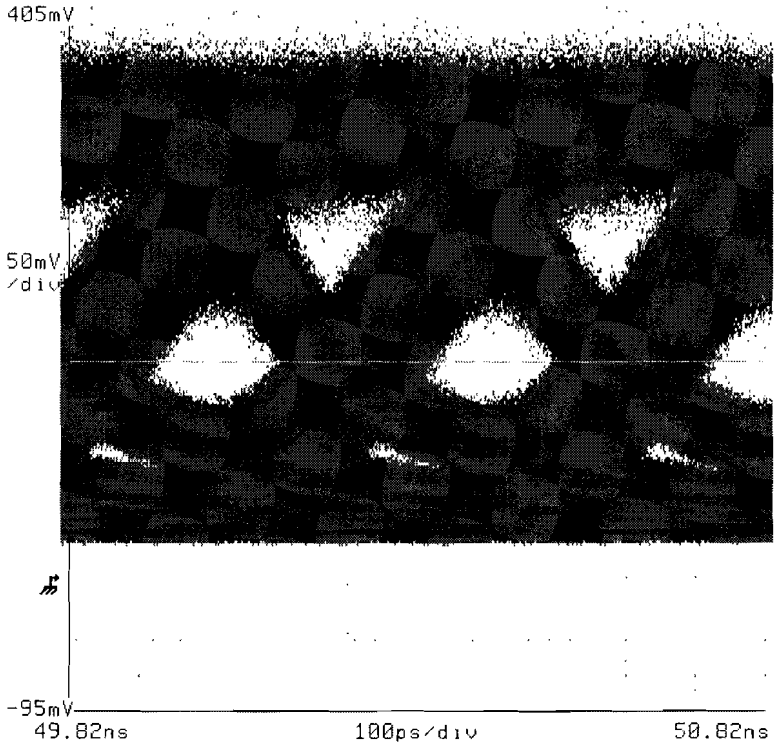

Figure 6.7: Eye diagram for 2.5 Gbit/s modulation. Error-free detection is achieved for this signal.

6.2.2 Determination of the Received Power for Error-Free Transmission

For 1.25 Gbit/s modulation, with the adjusted values for drive current (8.7 and 47.3 mA) the necessary received power for error-free transmission is determined. The input power remains -28 dBm, while the attenuation after the circulator increases. First the HP lightwave converter is used to detect the signals. The functionality can be seen as a regular photodiode with a transimpedance amplifier. The output is an exact representation of the optical input signal, in the electrical domain. The obtained BER for various received powers and two values of CW input power can be seen in figure 6.8. The difference between the measured point and a trendline through these points is low, so the measurements are reliable. The received power for error-free transmission with input power of -28 dBm is -14.3 dBm. The time-averaged gain in this case is 20.3 dB. For input power of -24 dBm, the received power for error-free detection drops to -15.9 dBm.

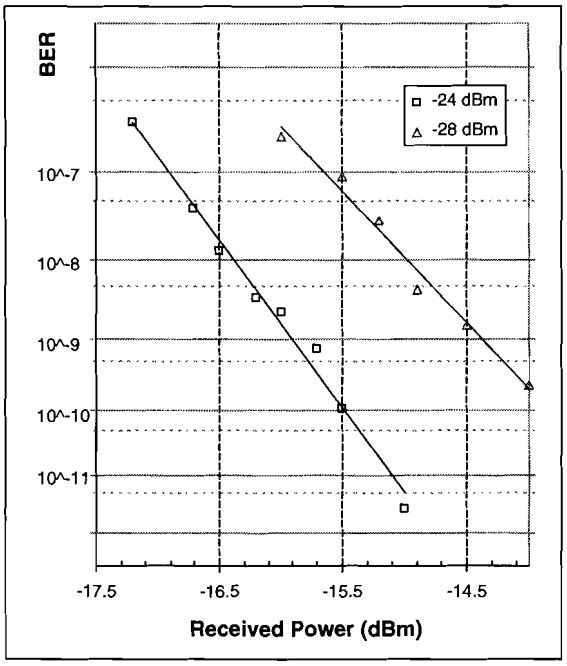

Figure 6.8: BER as a function of received power. A lightwave converter is used for detection of the signals.

Also measurements are performed with a 1.25 Gbit/s transceiver module. This module has an extra hard limiter, which leads to much better performance. The sensitivity of this module is -21 dBm. The BER curve in figure 6.9 shows received powers for error-free transmission between -24 and -25.5, which are all below the receiver sensitivity. This explains why the measured values of BER cannot be connected by a straight line. Measurements are performed for 4 values of input power.

6.3 Matching of the Measured Eye-Diagram

Since the difference between the dynamic simulation results of the MQW RSOA device and the dynamic measurements is quite severe, it is beneficial to design a new set of model parameters which gives a good representation of the dynamic measurements. This model will be applied in simulations of the entire network. The obtained eye-diagram and time-averaged gain from the dynamic measurements are target for the simulation results. It appeared to be very difficult to

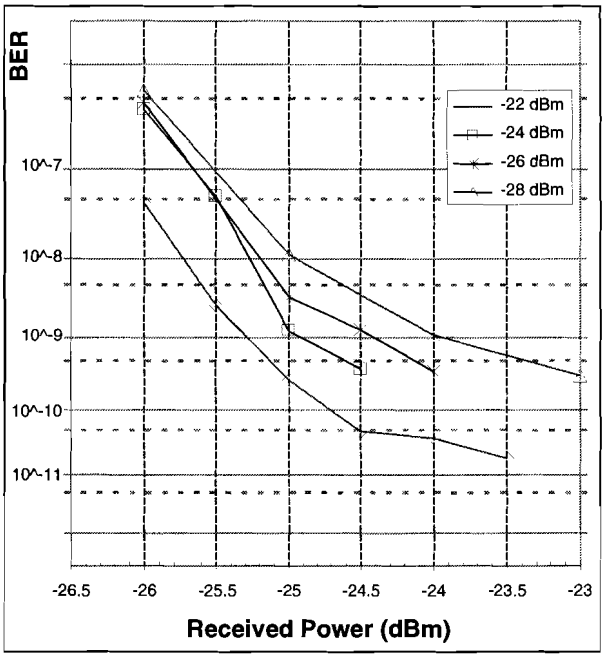

Figure 6.9: BER as function of received power. A 1.25 Gbit/s transceiver module is used for detection.

obtain quick rising slopes in combination with low noise. A complete match of the eye diagram is almost impossible, so a similar eye-diagram is generated, and the absolute powers are adjusted afterwards. This way the targeted eye diagram and average gain are obtained in the simulations. Figure 6.10 shows the simulated eye-diagram. To adjust the output power, an extra attenuation of 10 dB is applied. The model parameters for this case are shown in table 6.1.

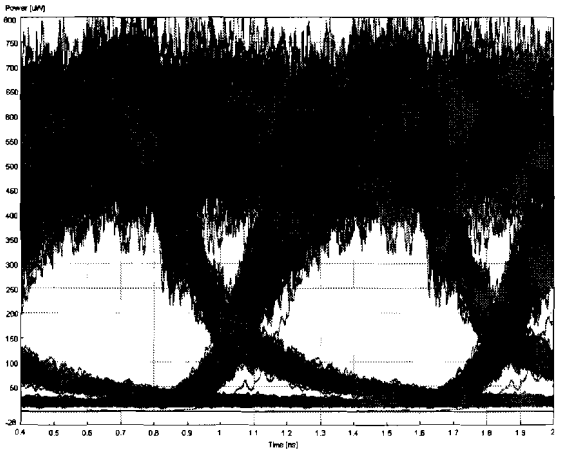

Figure 6.10: Simulated eye diagram which is matched to the measured eye diagram.

Symbol	Value	Unit
L	505.56e-6	m
w	1.2e-6	m
d_{MQW}	0.056e-6	m
$d_{HalfSCH}$	0.059e-6	m
Γ_{MQW}	0.045	
$\Gamma_{HalfSCH}$	0.2	
n_g	3.0	
R_l	1e-7	
R_r	0.3	
η_{opt}	0.5	
α_{i0}	1000.0	m^{-1}
η_{inj}	1.0	
A	0	s^{-1}
B	2.0e-18	m^3s^{-1}
C	1.3e-41	m^6s^{-1}
a	6.7e-20	m^2
N_0	2.0e24	m^{-3}
ε	1.0e-22	m^3
τ_ε	200e-15	s
τ_{cap}	70.0e-12	s
τ_{esc}	140.0e-12	s
δf	1.0e13	Hz
δf_{sp}	4.7e12	Hz
β	5e-4	

Table 6.1: Values for model parameters used in the simulations matched to the measured eye-diagram. After this MQW RSOA with these parameter values, an external attenuation of 10 dB has to be placed to obtain correct results.

Chapter 7

Conclusions and Recommendations

Now the dynamic simulations have been performed, the functionality of a reflective SOA as modulator of incoming CW-signal is shown. This means that the assignment of this project is completed and conclusions can be drawn from the performed simulations and measurements. However the project is finished, the implementation of some recommendations can improve the value of the obtained results.

7.1 Conclusions

When comparing the simulations and measurements of the bulk TW-SOA it can clearly be seen that large differences occur in both results. The simulated value for transparency current is much lower than the measured value, and the gain that can be obtained is higher for the simulations than for the measurements. Also in the gain-current graph from figure 4.3 saturation effects are more present compared to the graph of figure 3.2.

In contradiction to this, the simulation results and measurement result of the MQW RSOA show good correspondence for some criteria. The transparency current is almost equal for both cases, and also both measurement and simulation show high obtainable gain. However cavity resonances are severely disturbing the results of the simulations of the saturation characteristics, for output powers beyond the saturation output power, the measured results are very similar to the simulated results.

When the differences between the measured static results and the simulated results are tried to be solved, it appeared to be very hard to find a set of parameters which gave simulation results exactly equal to the measurement results. It is difficult to find the exact influence of every parameter, due to the complicated model which is used in the simulations, and the limited information which could be found on this model. Also the large number of parameters that can be adjusted makes it even harder to obtain a good matching. Furthermore, the lack of detailed knowledge of device parameters does not contribute to easy matching.

Generally, the simulations give a good qualitative representation of the phenomena taking place in the SOA. Saturation and cavity resonances are clearly present in the model. However the achievable modulation speed is different between the simulations and measurements, the simulated eye-diagrams look much like the measured eye-diagrams. Also pattern-effects and chirping are represented correctly.

The dynamic measurements show surprisingly good results for the MQW RSOA. The high gain and high extinction ratio are above expectations. Also the achievable modulation rate is very satisfying, especially keeping in mind that the drive current swing is only 40 mA. The project requirements for modulation speed, achievable gain and input power will not be a problem. On the other hand, the performance on the extinction rate and OSNR has to be improved. The achievable data-rate with larger current swing is expected to be around 3 Gbit/s, but not much higher, so the data-rate which was proposed in the original project plan [1], 10 Gbit/s will not be obtained with this device.

7.2 Recommendations

The large polarisation dependence of the MQW RSOA is not beneficial. For application in Fiber-to-the-Home networks, all components should preferably be polarisation independent. A new commercially available MQW RSOA device shows low polarisation dependence (SOA-RL-OEC-1550 by CIP). It is recommended that this device is also tested. This will also gain insight in the importance of this issue. By evaluating the performance of this new device, requirements on polarisation dependence can be introduced and justified.

All measurements until now are performed with optical input power, without any noise imposed on it. For a better representation of the real system, measurements and simulations have to be performed with input signals containing noise. This will lead to more stringent requirements on the performance of the RSOA. The results from these simulations and measurements will also justify the requirements on OSNR as defined in Deliverable 1.3 [14]. For the simulations, the model parameters described in section 6.3 can be used.

In order to obtain higher modulation speed, other materials have to be investigated, preferably Quantum Dot material. It is known that QD devices have quick responses, but the direct modulation properties of QD devices are relative unknown. Also the limitations of modulation speed, caused by cavity length and parasitic capacitance have to be taken into account in this investigation, making it a complex job.

Bibliography

[1] H. de Waardt and A.M.J. Koonen. BBPhotonics, dynamically reconfigurable broadband photonic access networks, October 2004. restricted.

[2] P.J. Urban, E.G.C. Pluk, A.M.J. Koonen, G.D. Khoe, and H. de Waardt. First design of dynamically reconfigurable broadband photonic access networks. In *Proc. 10th IEEE/LEOS Symposium - Benelux chapter*, pages 117 – 120, Mons, Belgium, 1-2 December 2005.

[3] G.N. van den Hoven, P. Stassar, C.G.H. Roeloffzen, R. Roy, G. Manhoudt, A.M.J. Koonen, and H. de Waardt. D1.2; prelimidary specifications of systems components and modules, BBPhotonics project deliverable, april 2005. restricted.

[4] M.D. Feuer, J.M. Wiesenfeld, J.S. Perino, C.A. Burrus, G. Raybon, S.C. Shunk, and N.K. Dutta. Single-port laser-amplifier modulators for local access. *IEEE Photonics Technology Letters*, 8(9):1175 – 1177, September 1996.

[5] N.J. Frigo, P.P.Iannone, P.D. Magill, T.E. Darcie, M.M. Downs, B.N. Desai, U. Koren, T.L. Koch, C. Dragone, H.M. Presby, and G.E. Bodeep. A wavelength-division multiplexed passive optical network with cost-shared components. *IEEE Photonics Technology Letters*, 6(11):1365 – 1367, November 1994.

[6] P. Healey, P. Townsend, C. Ford, L. Johnston, P. Townley, I. Lealman, L. Rivers, S. Perrin, and R.Moore. Spectral slicing WDM-PON using wavelength-seeded reflective SOAs. *Electronics Letters*, 37(19):1181 – 1182, September 2001.

[7] N. Buldawoo, S. Mottet, H. Dupont, D. Sigogne, and D. Meichenin. Transmission experiment using a laser amplifier-reflector for DWDM access network. In *Proc. of the European Conference on Optical Communication (ECOC)*, pages 273 – 274, Madrid, Spain, 20-24 September 1998.

[8] J.J. Koponen and M.J. Söderlund. A duplex WDM passive optical network with 1:16 power split using reflective SOA remodulator at ONU. In *Proc. of the Optical Fiber Communication Conference (OFC)*, MF99, Los Angeles, California, USA, 22 - 27 February 2004.

[9] H. Takesue and T. Sugie. Wavelength channel data rewrite using saturated SOA modulator for WDM networks with centralized light sources. *Journal of Lightwave Technology*, 21(11):2546 – 2556, November 2003.

[10] H.C. Shin, J.S. Lee, I.K. Yun, S.W. Kim, H.I. Kim, H.S. Shin, S.T. Hwang, Y.J. Oh, Y.K. Oh, and C.S. Shim. Reflective SOAs optimized for 1.25 [g.

[11] F.-T. An, K.S. Kim, D. Gutierrez, S. Yam, E. Hu, K. Shrikhande, and L.G. Kazovsky. SUCCESS: A next-generation hybrid WDM/TDM optical access network architecture. *Journal of Lightwave Technology*, 22(11):2557 – 2569, November 2004.

[12] J. Prat, C. Arellano, V. Polo, and C. Bock. Optical network unit based on a bidirectional reflective semiconductor optical amplfier for Fiber-to-the-Home networks. *IEEE Photonic Technology Letters*, 1(17):250 - 252, January 2005.

[13] E. Wong, K.L. Lee, and T. Anderson. Directly-modulated self-seeding reflective SOAs as colorless transmitters for WDM passive optical networks. In *Proc. of the Optical Fiber Communications Conference (OFC)*, PDP49, Anaheim, California, USA, 5-10 March 2006.

[14] A.M.J. Koonen, P.J. Urban, E.G.C. Pluk, H. de Waardt, and G.N. van den Hoven. D1.3; first design of reconfigurable access network, first specifications for components and modules, BBPhotonics project deliverable, December 2005. resticted.

[15] A. Yariv. *Optical Electronics in Modern Communications.* New York, Oxford University Press, fifth edition, 1997.

[16] G.P. Agrawal and N.K. Dutta. *Long-Wavelength Semiconductor Lasers.* New York, Van Nostrand Reinhold Company, 1986.

[17] N.K. Dutta and R.J. Nelson. The case for auger recombination in $In_{1-x}Ga_xAs_yP_{1-y}$. *Journal of Applied Physics*, 53(1):74 - 92, January 1982.

[18] VPIphotonics. *Active Photonics User's Manual*, July 2004. Chapter 5.

[19] T.P. Lee. Effect of junction capacitance on the rise time of LED's and on the turn-on delay on injection lasers. *The Bell System Technical Journal*, 54(1):53 - 68, January 1975.

[20] P.B. Johns and R.L. Beurle. Numerical modelling of 2-dimensional scattering problems using a transmission line matrix. *Proceedings of IEE*, 118(9):1203 – 1208, September 1971.

[21] W.J.R. Hoefer. The transmission-line matrix method - theory and applications. *IEEE Transactions on Mictowave Theory and Techniques*, 33(10):882 – 893, October 1985.

[22] A.J. Lowery. Transmission-line modelling of semiconductor lasers: The tranmission-line laser model. *International Journal of Numerical Modelling, Electronic Networks, Devices and Fields*, 2(4):249 – 265, 1989.

[23] F. Lealman I, L.J. Rivers, M.J. Harlow, and S.D. Perrin. InGaAsP/InP tapered active layer multiquantum well laser with 1.8 dB coupling loss to cleaved singlemode fibre. *Electronics Letters*, 30(20):1685 – 1687, September 1994.

[24] I.F. Lealman, A.E. Kelly, L.J. Rivers, S.D. Perrin, and R. Moore. Improved gain block for long wavelength (1.55 μm) hybrid integrated devices. *Electronics Letters*, 34(23):2247 – 2249, November 1998.

Appendix A

Design of SOA Driver Cable

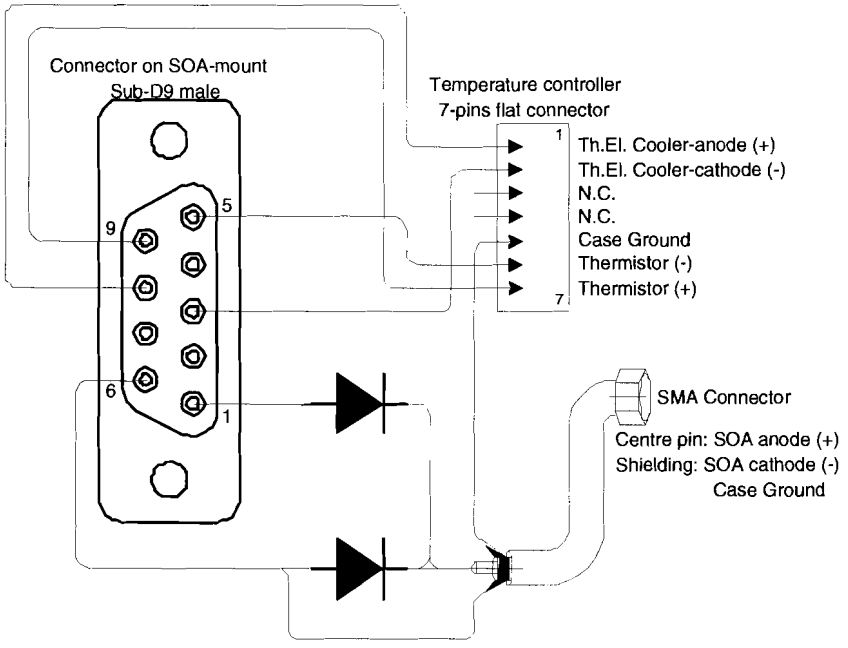

Figure A.1: Connection diagram within the SOA mount.

During this graduation project, two SOA driver cables were produced. The design of these cables is discussed in this appendix. The cable is designed for use with the laser diode / temperature controller module ITC 8052 from Thorlabs. The cable can also be used for other ITC modules, or combinations of various LDC and TEC modules from Thorlabs. Figure A.2 shows the connection diagram of the SOA driver cable, while figure A.1 shows the layout of the connections inside the RSOA mount.

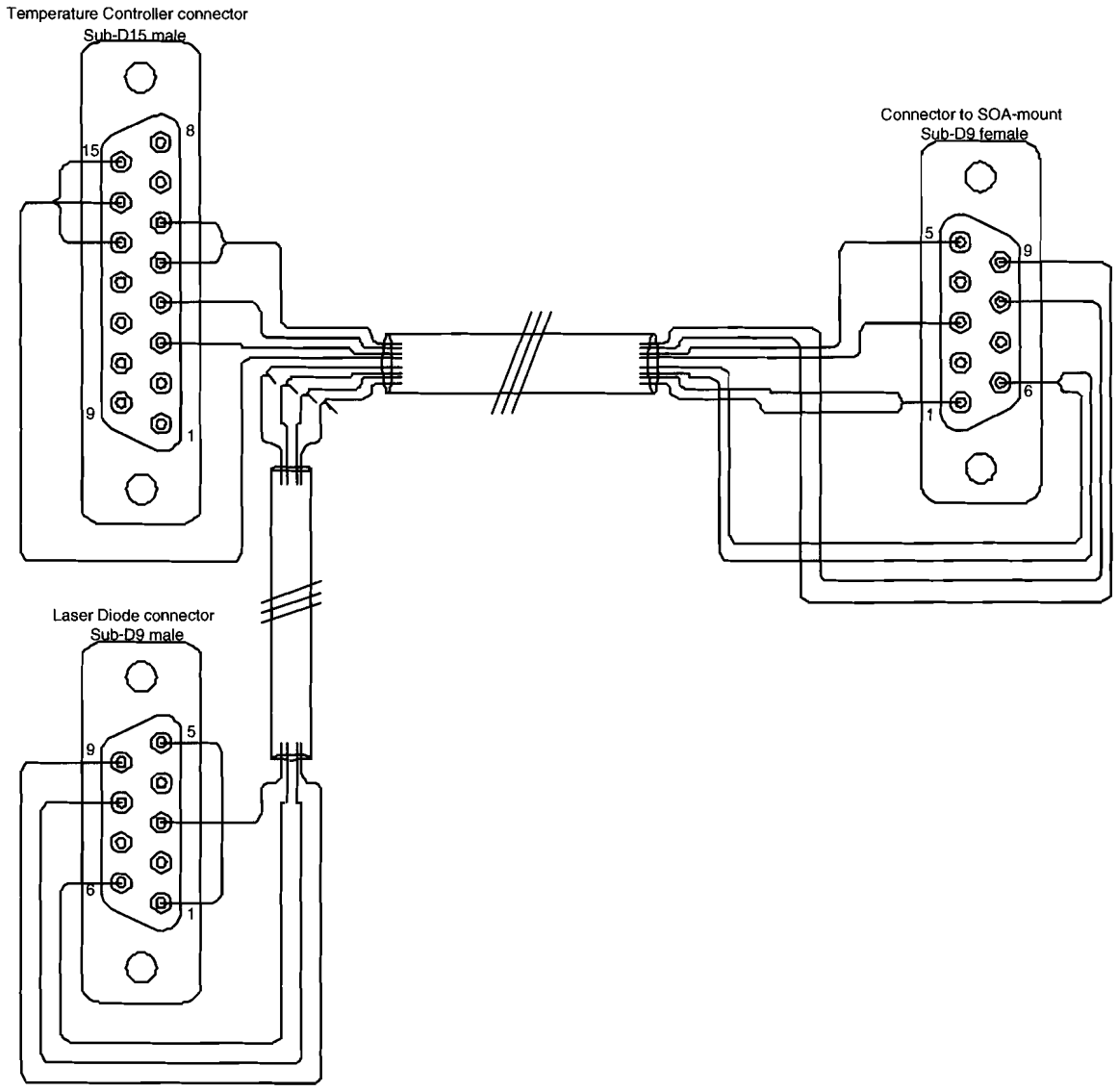

Figure A.2: Connection diagram of the SOA driver cable.

Appendix B

Simulation Results

P_{in} = -30 dBm				P_{in} = -20 dBm		
I (mA)	P_{out} (dBm)	G (dB)		I (mA)	P_{out} (dBm)	G (dB)
0	-72.043	-42.037		0	-62.036	-42.030
10	-52.611	-22.605		10	-42.607	-22.601
20	-39.887	-9.882		20	-29.907	-9.901
30	-30.394	-0.389		30	-20.448	-0.443
40	-22.617	7.388		40	-12.792	7.213
50	-16.048	13.957		50	-6.559	13.446
60	-10.464	19.542		60	-1.702	18.304
70	-5.753	24.253		70	1.693	21.698
80	-2.323	27.683		80	4.177	24.183
90	-0.486	29.520		90	5.933	25.938
100	1.493	31.499		100	7.175	27.180
110	3.387	33.393		110	8.080	28.086
120	4.928	34.933		120	8.795	28.801
P_{in} = -14 dBm				P_{in} = -10 dBm		
I (mA)	P_{out} (dBm)	G (dB)		I (mA)	P_{out} (dBm)	G (dB)
0	-56.013	-42.007		0	-51.967	-41.962
10	-36.594	-22.589		10	-32.569	-22.564
20	-23.924	-9.919		20	-19.958	-9.953
30	-14.565	-0.560		30	-10.785	-0.779
40	-7.242	6.764		40	-3.978	6.027
50	-1.784	12.222		50	0.655	10.660
60	1.983	15.989		60	3.647	13.652
70	4.470	18.475		70	5.657	15.662
80	6.187	20.193		80	7.099	17.105
90	7.474	21.479		90	8.201	18.206
100	8.492	22.497		100	9.086	19.091
110	9.328	23.333		110	9.823	19.829
120	10.032	24.037		120	10.455	20.461

Table B.1: Simulation results for the gain-current characterisation of the bulk TW-SOA, without matching.

I = 70 mA			I = 100 mA		I = 120 mA	
-50.005	-23.819	26.186	-14.907	35.098	-10.561	39.445
-48.005	-22.290	25.715	-13.423	34.582	-9.084	38.921
-46.005	-20.623	25.382	-11.808	34.197	-7.469	38.536
-44.006	-18.855	25.150	-10.104	33.902	-5.756	38.250
-42.005	-17.018	24.987	-8.347	33.658	-3.984	38.021
-40.005	-15.138	24.868	-6.574	33.431	-2.199	37.807
-38.005	-13.235	24.770	-4.818	33.187	-0.453	37.552
-36.005	-11.327	24.678	-3.109	32.896	1.182	37.187
-34.006	-9.432	24.574	-1.475	32.530	2.636	36.642
-32.005	-7.566	24.439	0.063	32.068	3.879	35.884
-30.005	-5.753	24.253	1.493	31.499	4.928	34.933
-28.005	-4.017	23.989	2.819	30.825	5.828	33.833
-26.005	-2.385	23.620	4.057	30.062	6.626	32.631
-24.006	-0.882	23.124	5.229	29.234	7.361	31.366
-22.005	0.479	22.485	6.323	28.328	8.072	30.078
-20.005	1.693	21.698	7.175	27.180	8.795	28.801
-18.005	2.762	20.767	7.734	25.739	9.409	27.414
-16.005	3.687	19.693	8.144	24.150	9.775	25.780
-14.006	4.470	18.475	8.492	22.497	10.032	24.037
-12.005	5.118	17.123	8.806	20.812	10.252	22.258
-10.005	5.657	15.662	9.086	19.091	10.455	20.461

Table B.2: Simulation results for the saturation characterisation of the bulk TW-SOA, without matching.

P_{in} = -30 dBm			P_{in} = -20 dBm		
I (mA)	P_{out} (dBm)	G (dB)	I (mA)	P_{out} (dBm)	G (dB)
0	-38.160	-8.155	0	-28.281	-8.277
10	-23.544	6.461	10	-14.131	5.874
20	-7.432	22.573	20	-1.159	18.846
30	-1.317	28.688	30	3.670	23.675
40	2.380	32.385	40	5.626	25.631
50	4.176	34.181	50	7.131	27.136
60	5.073	35.078	60	8.229	28.234
70	5.397	35.402	70	9.471	29.476
80	5.273	35.278	80	10.154	30.159
P_{in} = -14 dBm			P_{in} = -10 dBm		
I (mA)	P_{out} (dBm)	G (dB)	I (mA)	P_{out} (dBm)	G (dB)
0	-22.514	-8.509	0	-18.940	-8.935
10	-9.482	4.523	10	-7.076	2.929
20	0.819	14.824	20	1.633	11.638
30	4.583	18.588	30	4.948	14.953
40	6.625	20.630	40	6.861	16.866
50	8.027	22.032	50	8.211	18.216
60	9.087	23.092	60	9.265	19.270
70	9.927	23.933	70	10.111	20.116
80	10.620	24.625	80	10.808	20.813

Table B.3: Simulation results for the gain-current characterisation of the MQW RSOA, without matching.

I = 30 mA				I = 50 mA			I = 80 mA	
-50.005	-15.2101	34.795		-14.5281	35.477		-5.97114	44.034
-48.005	-13.6855	34.319		-12.9687	35.036		-4.64775	43.357
-46.005	-12.0531	33.952		-11.2488	34.756		-3.27113	42.734
-44.006	-10.3815	33.624		-9.40191	34.603		-1.9261	42.079
-42.005	-8.7422	33.263		-7.44434	34.560		-0.67342	41.331
-40.005	-7.20354	32.801		-5.36088	34.644		0.468786	40.474
-38.005	-5.80849	32.196		-3.02722	34.977		1.524345	39.529
-36.005	-4.56272	31.442		0.723589	36.728		2.513803	38.519
-34.006	-3.43707	30.568		3.134792	37.140		3.459262	37.464
-32.005	-2.3812	29.624		3.706434	35.711		4.374014	36.379
-30.005	-1.31712	28.688		4.175705	34.181		5.272815	35.278
-28.005	0.03606	28.041		4.63353	32.638		6.229732	34.234
-26.005	2.00793	28.013		5.156711	31.162		8.962165	34.967
-24.006	2.396103	26.401		6.726433	30.732		9.182949	33.188
-22.005	2.781221	24.786		6.910647	28.915		9.414957	31.420
-20.005	3.669676	23.675		7.131326	27.136		10.15351	30.159
-18.005	3.935167	21.940		7.657296	25.662		10.25206	28.257
-16.005	4.183071	20.188		7.766738	23.772		10.5519	26.557
-14.006	4.583369	18.588		8.026684	22.032		10.61989	24.625
-12.005	4.74506	16.750		8.113852	20.119		10.69141	22.696
-10.005	4.9476	14.953		8.210991	18.216		10.80812	20.813

Table B.4: Simulation results for the saturation characterisation of the MQW RSOA, without matching.

P_{in} = -20 dBm				P_{in} = -10 dBm		
I (mA)	P_{out} (dBm)	G (dB)		I (mA)	P_{out} (dBm)	G (dB)
10	-43.999	-23.993		10	-33.981	-23.976
20	-36.340	-16.334		20	-26.346	-16.341
30	-30.569	-10.564		30	-20.605	-10.599
40	-25.802	-5.797		40	-15.894	-5.889
50	-21.702	-1.697		50	-11.874	-1.869
60	-18.081	1.924		60	-8.376	1.629
70	-14.818	5.187		70	-5.314	4.692
80	-11.834	8.172		80	-2.635	7.370
90	-9.108	10.898		90	-0.326	9.680
100	-6.615	13.391		100	1.634	11.639
110	-4.303	15.702		110	3.287	13.292
120	-2.192	17.813		120	4.681	14.686

Table B.5: Simulation results for the bulk SOA, with matching.

P_{in} = -30 dBm				P_{in} = -20 dBm		
I (mA)	P_{out} (dBm)	G (dB)		I (mA)	P_{out} (dBm)	G (dB)
10	-25.882	4.136		10	-16.458	3.561
15	-17.939	12.079		15	-9.660	10.359
20	-12.172	17.846		20	-5.535	14.483
25	-8.160	21.858		25	-2.982	17.036
30	-5.493	24.525		30	-1.230	18.788
35	-3.525	26.493		35	0.021	20.040
40	-2.239	27.779		40	1.011	21.029
45	-1.143	28.876		45	1.788	21.806
50	-0.222	29.796		50	2.415	22.434
55	0.518	30.536		55	2.952	22.971
60	1.090	31.109		60	3.419	23.437
65	1.586	31.604		65	3.829	23.847
70	1.997	32.015		70	4.192	24.210
75	2.391	32.409		75	4.520	24.538
80	2.718	32.736		80	4.805	24.823

Table B.6: Simulation results for the bulk SOA, with matching.

Appendix C

Measurement Results

P_{in} = -20 dBm; 15°C				P_{in} = -20 dBm; 25°C		
I (mA)	P_{out} (dBm)	G (dB)		I (mA)	P_{out} (dBm)	G (dB)
10	-65.6	-43.85		10	-66.85	-45.1
20	-46.55	-24.8		20	-56	-34.25
30	-31.4	-9.65		30	-39.75	-18
40	-22.5	-0.75		40	-29.75	-8
50	-16.5	5.25		50	-22.9	-1.15
60	-12.3	9.45		60	-18	3.75
70	-9.2	12.55		70	-14.3	7.45
80	-6.85	14.9		80	-11.4	10.35
90	-5	16.75		90	-9.15	12.6
100	-3.6	18.15		100	-7.3	14.45
110	-2.4	19.35		110	-5.8	15.95
120	-1.4	20.35		120	-4.6	17.15
P_{in} = -10 dBm; 15°C				P_{in} = -10 dBm; 25°C		
I (mA)	P_{out} (dBm)	G (dB)		I (mA)	P_{out} (dBm)	G (dB)
10	-64.6	-53.45		10	-66.2	-55.05
20	-36.2	-25.05		20	-46.5	-35.35
30	-21	-9.85		30	-29.35	-18.2
40	-12.3	-1.15		40	-19.35	-8.2
50	-6.85	4.3		50	-12.7	-1.55
60	-3.2	7.95		60	-8.1	3.05
70	-0.7	10.45		70	-4.7	6.45
80	1.2	12.35		80	-2.2	8.95
90	2.6	13.75		90	-0.3	10.85
100	3.7	14.85		100	1.2	12.35
110	4.6	15.75		110	2.4	13.55
120	5.35	16.5		120	3.35	14.5

Table C.1: Measurement results for the gain-current characterisation of the bulk TW-SOA. Compensation for isolator loss is applied before the calculation of the gain.

I = 100 mA; 15°C				I = 100 mA; 25°C		
P_{in} (dBm)	P_{out} (dBm)	G (dB)		P_{in} (dBm)	P_{out} (dBm)	G (dB)
-40	-19.8	21.45		-40	-23.4	17.85
-35	-16.85	19.4		-35	-20.7	15.55
-30	-12.8	18.45		-30	-16.75	14.5
-28	-11	18.25		-28	-14.95	14.3
-26	-9.2	18.05		-26	-13.1	14.15
-24	-7.35	17.9		-24	-11.25	14
-22	-5.55	17.7		-22	-9.4	13.85
-20	-3.8	17.45		-20	-7.55	13.7
-18	-2.2	17.05		-18	-5.75	13.5
-16	-0.7	16.55		-16	-4.05	13.2
-14	0.6	15.85		-14	-2.5	12.75
-12	1.75	15		-12	-1.05	12.2
-10	2.65	13.9		-10	0.2	11.45
-8	3.45	12.7		-8	1.3	10.55
-6	4.1	11.35		-6	2.15	9.4
-4	4.6	9.85		-4	2.9	8.15
-2	5	8.25		-2	3.5	6.75
0	5.35	6.6		0	4	5.25
2	5.6	4.85		2	4.4	3.65

Table C.2: Measurement results for the saturation characterisation of the bulk TW-SOA. Compensation for isolator loss is applied before the calculation of the gain.

P_{in} = -30 dBm; 20°C				P_{in} = -20 dBm; 20°C		
I (mA)	P_{out} (dBm)	G (dB)		I (mA)	P_{out} (dBm)	G (dB)
7				7	-35.835	-15.835
10	-30.844	-0.824		10	-21.043	-1.043
15	-16.801	13.219		15	-7.972	12.028
20	-10.951	19.069		20	-2.666	17.334
25	-7.696	22.324		25	-0.070	19.930
30	-5.636	24.384		30	1.632	21.632
35	-4.408	25.612		35	2.772	22.772
40	-3.622	26.398		40	3.675	23.675
45	-3.164	26.856		45	4.310	24.310
50	-2.682	27.338		50	4.827	24.827
55	-2.371	27.649		55	5.289	25.289
60	-2.071	27.949		60	5.657	25.657
65	-1.701	28.319		65	5.928	25.928
70	-1.431	28.589		70	6.233	26.233
75	-1.161	28.859		75	6.417	26.417
80	-1.021	28.999		80	6.588	26.588

Table C.3: Measurement results for the gain-current characterisation of the MQW RSOA. Compensation for coupler loss is already applied at the displayed values of output power.

$I = 30$ mA		
P_{in} (dBm)	P_{out} (dBm)	G (dB)
-38.19	-13.407	24.783
-35.12	-10.468	24.652
-32.27	-7.744	24.526
-29.69	-5.394	24.296
-27.08	-3.107	23.973
-25.11	-1.658	23.452
-22.39	0.221	22.611
-19.26	2.003	21.263
-16.76	3.104	19.864
-14.55	3.891	18.441
-12.14	4.524	16.664
-9.72	4.989	14.709
-7.39	5.290	12.680
-4.37	5.536	9.906

$I = 50$ mA		
P_{in} (dBm)	P_{out} (dBm)	G (dB)
-38	-10.568	27.432
-36	-8.537	27.463
-33.38	-6.056	27.324
-29.47	-2.261	27.209
-27.2	-0.294	26.906
-24.29	2.175	26.465
-21.87	3.826	25.696
-19.59	5.083	24.673
-17.29	6.078	23.368
-15.42	6.727	22.147
-12.21	7.541	19.751
-9.66	7.997	17.657
-7.42	8.267	15.687
-5.16	8.439	13.599

$I = 80$ mA		
P_{in} (dBm)	P_{out} (dBm)	G (dB)
-38.22	-9.180	29.040
-34.92	-5.849	29.071
-29.95	-0.981	28.969
-26.87	1.726	28.596
-24.52	3.730	28.250
-22.57	5.056	27.626
-19.41	6.950	26.360
-17.27	7.876	25.146
-14.82	8.768	23.588
-12.34	9.448	21.788
-9.66	9.947	19.607

Table C.4: Measurement results for the saturation characterisation of the MQW RSOA. Compensation of coupler loss is already applied at the displayed values of power.